NIST Technical Note
NIST TN 2275

A Practical Computational Fluid Dynamics Approach for Structural Engineering: Simulation of Approach Flow with Reduced Blockage Ratios

Yunjae Hwang
DongHun Yeo

This publication is available free of charge from:
https://doi.org/10.6028/NIST.TN.2275

NIST NATIONAL INSTITUTE OF STANDARDS AND TECHNOLOGY
U.S. DEPARTMENT OF COMMERCE

NIST Technical Note
NIST TN 2275

A Practical Computational Fluid Dynamics Approach for Structural Engineering: Simulation of Approach Flow with Reduced Blockage Ratios

Yunjae Hwang
PREP Associate
Materials and Structural Systems Division
Engineering Laboratory
NIST
Department of Mechanical Engineering
Johns Hopkins University

DongHun Yeo
Materials and Structural Systems Division
Engineering Laboratory
NIST

This publication is available free of charge from:
https://doi.org/10.6028/NIST.TN.2275

November 2023

U.S. Department of Commerce
Gina M. Raimondo, Secretary

National Institute of Standards and Technology
Laurie E. Locascio, NIST Director and Under Secretary of Commerce for Standards and Technology

NIST TN 2275
November 2023

Publication History
Approved by the NIST Editorial Review Board on 2023-10-30

How to Cite this NIST Technical Series Publication
Hwang Y, Yeo D (2023) A Practical Computational Fluid Dynamics Approach for Structural Engineering: Simulation of Approach Flow with Reduced Blockage Ratios. (National Institute of Standards and Technology, Gaithersburg, MD), NIST Technical Note (TN) NIST TN 2275. https://doi.org/10.6028/NIST.TN.2275

NIST Author ORCID iDs
Yunjae Hwang: 0000-0003-2697-5319
DongHun Yeo: 0000-0002-8019-9624

Contact Information
donghun.yeo@nist.gov

Abstract

Computational fluid dynamics (CFD) simulations for structural wind engineering applications require a fully developed boundary layer approach flow with horizontal homogeneity and zero pressure gradient for accurate characterization of wind loading on a structure. Previous studies have focused on achievement of such requirements primarily in computational domains whose heights are equal to or less than the atmospheric boundary layer (ABL) height, despite the need of a computational domain taller than the ABL height for certain applications such as buildings in an urban environment/or topographic surroundings to ensure an acceptably low blockage ratio. Thus, the current study proposes a novel procedure incorporating a body force for the generation of fully developed, horizontally homogeneous flow with a zero pressure gradient in a vertically extended computational domain above the ABL height using Reynolds-averaged Navier-Stokes (RANS) simulations. The proposed procedure is applied to simulations with an isolated building and topographic models, respectively, to investigate the blockage effects on the flow field in the vicinity of the models and associated wind loading on their surfaces. The results demonstrate successful creation of the approach flow that satisfies those three requirements for CFD simulations in structural wind engineering and applicability to scale-resolving CFD simulations including large-eddy simulations (LES).

Keywords

Approach flow simulation; atmospheric boundary layer (ABL); blockage ratio; computational fluid dynamics (CFD); horizontal homogeneity; horizontal pressure gradient; Reynolds-averaged Navier-Stokes (RANS); structural engineering; wind engineering.

Table of Contents

List of Tables

List of Figures

Author Contributions

Yunjae Hwang: Data curation, Formal analysis, Software, Validation, Visualization, Writing- Original draft preparation; DongHun Yeo: Conceptualization, Methodology, Supervision, Writing- Reviewing and Editing.

1. Introduction

Computational fluid dynamics (CFD) approach has gained attention in studying wind engineering applications due to its advantages over experimental techniques. In contrast to experiments, CFD simulations can provide field quantities at any location in the computational domain without disturbing the flow by measurement equipment, and the simulations have fewer limitations in testing conditions, e.g., scaling of a model, domain size, and boundary conditions. Among many challenges, however, it remains difficult to reproduce the characteristics of atmospheric boundary layer (ABL) wind in a computational domain, particularly for a turbulent wind profile over a rough terrain. To accurately estimate the wind fields around structures and associated aerodynamic effects on their surfaces in structural wind engineering applications, the ABL flow in an empty computation domain should be fully developed and horizontally statistically homogeneous with a zero pressure gradient in the along-wind direction. Therefore, many efforts have been made to generate approach flows that satisfy such requirements.
Richards and Hoxey (1993) first obtained a shear-stress driven ABL flow in a computational domain by applying a constant shear stress on the top boundary together with specifying the inflow profiles of a fully developed flow (i.e., velocity, turbulence kinetic energy [k] and turbulence dissipation [ε]) at the inlet. However, the suggested method produces a constant shear stress profile over the height, which could be a reasonable approximation for only the lower part of the ABL but not for the full ABL height. Subsequent studies have focused on development of approach flow up to its full ABL height featuring not only horizontal homogeneity but also a shear stress profile that is more realistic than a constant shear stress. One approach is to modify a set of governing equations or relevant turbulence model parameters. Yang et al. (2009) modified the profiles of k and ε to achieve the horizontal homogeneity. Parente et al. (2011a; 2011b) proposed a simulation with modified governing equations of the standard k-ε model, in addition to inlet boundary condition representing a fully developed flow. However, when either model parameters or governing equations are modified, it is crucial to evaluate the potential effects on the simulation results (e.g., flow characteristics in a region of interest and pressure distribution on a building) (Richards & Norris, 2019). Moreover, those simulations generate a negative pressure gradient in the along-wind direction in the computational domain for the horizontally homogeneous flow. Such a pressure gradient is not desired in simulations for structural applications requiring accurate estimation of wind loading on a structure, as a homogeneous pressure field is pursued in wind tunnel tests (ASCE, 2021). To address these challenges, another approach incorporating an additional body-force in the momentum equation was proposed (Cai, et al., 2014; Cindori, et al., 2018; Cindori, et al., 2020; Shi & Yeo, 2017). The extra term acts as a driving force for ABL flow instead of the pressure gradient, which is the driving mechanism of the approach flow in the methods mentioned above, this allowing a zero pressure gradient to be achieved along the fetch. More importantly, this alternative approach is not limited to a specific turbulence model or set of simulation parameters, unlike previous techniques.
Another challenge in wind engineering simulations is ensuring that the blockage ratio in the computational domain remains at an acceptably low level, commonly suggested as 3% (Franke, et al., 2007; Tominaga, et al., 2008), to prevent acceleration of the flow field due to a high blockage ratio. Because most previous CFD simulations have focused on relatively small structures in a computational domain whose height is equal to or less than the ABL height (Richards & Hoxey, 1993), and because the blockage ratio can be reduced by laterally extending the computational domain, blockage effects on flow fields and aerodynamics of structures have

not received much attention in structural wind engineering communities. However, a simulation of a large group of buildings in an urban environment or a simulation of flow over mountainous terrain cannot achieve blockage ratios as low as the recommended value of 3 % by expanding the width of the computation domain, because other buildings may be present, or the elevation of the topography could still be significant in that extended domain. In such cases, the only option to lower the blockage ratio is to increase the height of the computational domain to include the free atmosphere beyond the ABL as part of the simulation. However, according to the authors' best knowledge, limited research has been performed for structural wind engineering applications to achieve horizontally homogeneous flow with a zero pressure gradient in the along-wind direction using a computational domain with vertical dimensions significantly greater than the ABL height (e.g., the domain height is a few times higher than the ABL height). A handful of studies with a constant pressure gradient were conducted in the field of meteorology, e.g., (van der Laan, et al., 2020; van der Laan, et al., 2021). Previous approaches for horizontally homogenous ABL flow generation, such as application of shear-driven flow to the top boundary (Richards & Hoxey, 1993; Richards & Norris, 2019), adoption of a body force in the whole domain (Cai, et al., 2014; Yeo & Shi, 2018; Kozmar, 2011; Cindori, et al., 2018; Cindori, et al., 2020), and employment of a flow rate at the inlet which induces a pressure gradient between the inlet and outlet boundaries (Richards & Norris, 2015; van der Laan, et al., 2020; van der Laan, et al., 2021), are not able to develop flow in a computational domain that includes boundary layer flow within the ABL height and free atmospheric flow above that height.

This research aims to develop a practical procedure to obtain approach flow conditions that satisfy the three major requirements for CFD simulations in structural wind engineering applications: (i) fully developed, horizontally homogeneous flow, (ii) zero pressure gradient in the streamwise direction, and (iii) acceptably low blockage ratio. The proposed approach in this study incorporates the body force determined from a target wind shear stress profile within the ABL height. The body force is in equilibrium with the friction force on the ground and is able to develop a fully developed, horizontally homogeneous flow. Two-stage simulations (i.e., precursor and main simulations) are used to investigate the effects of the simulation configuration for the approach flow on the flow and pressure fields of interest in structural wind engineering applications. The proposed CFD procedure successfully demonstrates the achievement of approach flow that complies with the major requirements for structural wind engineering applications.

The remainder of this report is organized as follows. Section 2 discusses the driving forces of ABL flow and their implementation in CFD simulations. Section 3 introduces governing equations and describes the computational configuration of simulations for structural engineering applications and then proposes a practical approach to obtain the target flow characteristics in a computational domain. Section 4 demonstrates four simulation cases to verify the proposed procedure. Section 5 summarizes the proposed procedure for its application to wind engineering problems. The last section summarizes the findings of the research and concludes with possible applications of the proposed method and future work.

2. Driving mechanism of the atmospheric boundary layer

The mean motion of wind in a neutrally stratified atmospheric boundary layer (ABL) can be described with balance of three dominant forces: horizontal pressure gradient, the Coriolis force and the divergence of shear stress (e.g., see Section 2.2 of (Simiu & Yeo, 2019)). Note that the current manuscript employs the cartesian coordinate system with *x*, *y* and *z* axes referring to the streamwise, lateral and vertical directions, respectively. *U*, *V* and *W* correspond to the mean wind speed of each direction and $|\boldsymbol{U}|$ is the velocity magnitude. If the curvature of the isobars is neglected, the balance between the three forces for the horizontal components of mean velocity can be written as,

$$\frac{1}{\rho}\frac{\partial p}{\partial x} - fV - \frac{1}{\rho}\frac{\partial \tau_{xz}}{\partial z} = 0, \tag{1}$$

$$\frac{1}{\rho}\frac{\partial p}{\partial y} + fU - \frac{1}{\rho}\frac{\partial \tau_{yz}}{\partial z} = 0, \tag{2}$$

where ρ is the density of air, p is the pressure, τ_{xz} and τ_{yz} are shear stress in the *xz* and *yz* planes, $f = 2\Omega\sin\phi$ is the Coriolis parameter with the angular velocity of Earth's rotation Ω and the latitude ϕ, respectively. On the left-hand side of Eqs. (1) and (2), the first term indicates the horizontal pressure gradient, as the primary driving forces of wind, which blows in the opposite directions to the pressure gradient. The second term represents the Coriolis force associated with the Earth's rotation. The last term represents the vertical change of shear stress, which acts as a retarding force that plays a significant role near the ground and reduces to zero at the top of the ABL. This means that the three components are balanced over the ABL height and the friction force has no influence above the ABL. Without friction, the horizontal velocity components of geostrophic wind in this free atmosphere U_g and V_g, in the *x* and *y* directions, respectively, can be expressed as

$$U_g = -\frac{1}{\rho f}\frac{\partial p}{\partial y}, \tag{3}$$

$$V_g = \frac{1}{\rho f}\frac{\partial p}{\partial x}. \tag{4}$$

For structural wind engineering applications, researchers generally have assumed that the veering of wind direction with height is negligible because the direction does not significantly alter in low elevations of the ABL, and the impact of the veering is not considerable in most practical applications (Deaves & Harris, 1978). Thus, unidirectional flow has been used in their computational domain. Such a simulation requires a driving force that balances with the loss of momentum due to the friction at the ground to sustain statistically steady and homogeneous ABL profiles in equilibrium. In this case, the representative form of the governing equation for the horizontal momentum can be expressed with,

$$\frac{1}{\rho}\frac{\partial p_{eff}}{\partial x} - \frac{1}{\rho}\frac{\partial \tau_{xz}}{\partial z} + f_b = 0, \tag{5}$$

where p_{eff} is the effective pressure (which neglects hydrostatic pressure effects), τ_{xz} is the shear stress in the xz plane, and f_b is the additional momentum source.

Equation (5) can be used to explain all approaches for horizontally homogeneous ABL flow simulations. These approaches can be classified into three groups depending on the driving mechanism used (i.e., horizontal pressure gradient (Richards & Norris, 2015), shear stress on the top boundary (Richards & Hoxey, 1993; Richards & Norris, 2019), and extra momentum source (Cai, et al., 2014; Cindori, et al., 2018; Cindori, et al., 2020)). Since Eq. (5) is a representative form, all of the individual terms do not need to be active and each component may be zero by itself depending on the driving mechanism of the ABL flow. The first possible scenario is that only the first two terms are of interest and the extra source does not exist, i.e., the change of shear stress in height z balances with the pressure gradient along the wind direction in x. Such balance is obtained either by directly applying the pressure difference between the inlet and outlet or by specifying volume flow rate at the inlet (e.g., (Richards & Norris, 2015)), which builds up non-zero pressure gradient field in an empty domain. However, it is not ideal that the pressure within the empty domain varies in the streamwise direction, particularly for structural wind engineering applications. Such a pressure gradient could lead to inaccurate predictions of pressure fields on the envelope of a structure and, consequently, the associated wind loads on the structure.

To achieve the horizontally zero pressure gradient (the first term in Eq. (5)) without any additional momentum source (f_b), the second component in that equation by itself should be zero as well. This is the case when shear force is applied to the top boundary to drive the boundary layer flow. This yields constant shear along the domain height and the horizontally homogeneous pressure condition is achieved. However, this method has two primary limitations. Firstly, a constant shear stress profile could be assumed in the lower part of ABL (also known as atmospheric surface layer) only. Thus, this approach is not suitable for simulations where the computational domain height is as tall as the ABL height. Secondly, such a low top boundary could cause significant blockage effects in certain wind engineering applications, such as simulations of urban environments and large-scale topography. Therefore, it is concluded that the zero pressure-gradient condition and realistic shear stress profile cannot be achieved at the same time without incorporating the additional momentum source term f_b. For this reason, an alternative approach adopts the extra source of momentum f_b as the driver of the ABL flow to achieve horizontal zero pressure gradient.

In this approach, the body force is usually assumed to be either linear or quadratic in height, depending on a target shear stress profile (Deaves & Harris, 1978; Richards & Norris, 2019; Cindori, et al., 2020). In this case, the change of the shear in height balances with the applied body force f_b and the change in pressure in the streamwise direction always remains zero. The driving force in a computational domain generated by the body force will be in equilibrium with the drag force on the ground boundary of the domain (Anderson & Meneveau, 2011). Since the body force used in this method can be derived from Eq. (5) with $\partial p_{\mathrm{eff}}/\partial x = 0$, the added body force in the governing equation takes the form of pressure gradient and is able to nullify the effective pressure gradient term (the first term in Eq. (5)) (Cindori, et al., 2020). This is analytically proven that the change of shear stress should be balanced with the added body force when there is no horizontal pressure gradient ($\partial p_{\mathrm{eff}}/\partial x = 0$). In other words, the shear stress is estimated by the integration of body force over the domain height, and this relationship is expressed as

$$f_b(z) = \frac{1}{\rho}\frac{d\tau_{zx}(z)}{dz}. \tag{6}$$

It is important to note that this relationship holds for any profiles of shear stress. For example, a linearly decreasing shear stress profile with height leads to a constant body force. A quadratically decreasing shear stress profile results in a linearly diminishing body force. This method is significantly more versatile than the other approaches because any specific target vertical shear stress profile can be achieved by defining the body force profile using Eq. (6).
Although the shape of shear stress profile $\tau(z)$ in the ABL is not defined in a unified form (IHS ESDU, 2001), it is recognized that the minimum and the maximum shear stresses occur at the top of the ABL and at the ground, respectively. The latter can be expressed as

$$\tau(z=0) = \sqrt{\tau_{xz}^2(0) + \tau_{yz}^2(0)} = \rho u_*^2, \tag{7}$$

where u_* is the friction velocity. Deaves and Harris (1978) modeled the shear as a parabolic profile,

$$\tau(z) = \rho u_*^2 \left(1 - \frac{z}{H_{ABL}}\right)^2, \tag{8}$$

where $H_{ABL}=u_*/(6f)$ is the approximate height of the ABL that has zero shear stress. On the other hand, Richards and Norris (2019) expressed the shear with a linear profile,

$$\tau(z) = \rho u_*^2 \left(1 + (\gamma - 1)\frac{z}{H_{ABL}}\right), \tag{9}$$

where γ is the ratio of shear stresses at the top and bottom of the domain. Thus, the shear stress profile will be constant for $\gamma=1$, but linear otherwise.
In the current study, we propose a practical approach based on a body force for developing a neutrally stratified ABL flow condition that is horizontally homogeneous with a zero pressure gradient in order to achieve the target shear stress profile. The body force profiles corresponding to linear and quadratic shear stress profiles are used for precursor simulations of approach flow. In the following main simulations, we investigate the effects of the body forces and simulation setup on flow and pressure fields of interest.

3. Configuration of approach flow simulation for structural wind engineering applications

This section introduces the computational fluid dynamics (CFD) simulation configuration for the body-force-driven ABL flow. As described in the previous section, this approach can generate horizontally homogeneous approach flow with a zero streamwise pressure gradient in an empty computation domain using a precursor simulation. The simulations in the current study are performed in a 2-D setting using Reynolds-averaged Navier-Stokes (RANS) with the standard k-ε turbulence model, but the approach is also applicable to 3-D Large Eddy Simulations (e.g., (Nandi & Yeo, 2021)).

The standard k-ε turbulence model solves the conservation of momentum equation (Eq. (5)), and the transport equations of turbulence kinetic energy (TKE, k) and the rate of TKE dissipation (ε) are expressed as:

k conservation:

$$\tau_{xz}\left(\frac{\partial U}{\partial z}\right)-\rho\varepsilon+\frac{\partial}{\partial z}\left(\frac{\mu_t}{\sigma_k}\frac{\partial k}{\partial z}\right)=0, \tag{10a}$$

$$\tau_{xz}\left(\frac{\partial W}{\partial z}\right)-\rho\varepsilon+\frac{\partial}{\partial z}\left(\frac{\mu_t}{\sigma_k}\frac{\partial k}{\partial z}\right)=0, \tag{10b}$$

ε conservation:

$$C_{\varepsilon 1}\tau_{xz}\left(\frac{\partial U}{\partial z}\right)\frac{\varepsilon}{k}-C_{\varepsilon 2}\rho+\frac{\partial}{\partial z}\left(\frac{\mu_t}{\sigma_\varepsilon}\frac{\partial \varepsilon}{\partial z}\right)=0, \tag{11a}$$

$$C_{\varepsilon 1}\tau_{xz}\left(\frac{\partial W}{\partial z}\right)\frac{\varepsilon}{k}-C_{\varepsilon 2}\rho+\frac{\partial}{\partial z}\left(\frac{\mu_t}{\sigma_\varepsilon}\frac{\partial \varepsilon}{\partial z}\right)=0, \tag{11b}$$

where U and W represent the flow velocity along the x and z axes, respectively; μ_t is the turbulent viscosity; and σ_k, $C_{\varepsilon 1}$, $C_{\varepsilon 2}$ and σ_ε are the modeling coefficients of the standard k-ε turbulence model. The U, k and ε profiles of the governing equations will be in equilibrium in the empty domain of the precursor simulation.

The precursor simulation employs periodic boundary conditions at the inlet and outlet. This creates a flow field that is equivalent to flow in an infinitely long domain in the horizontal direction for steady flow simulations. The periodic condition leads to a zero pressure gradient in the streamwise direction. In Eq. (5), thus, the first term is zero and the other remaining terms, which represent the vertical change of the shear stress and the momentum source, are active and balance each other. For a given shear stress profile (e.g., linear or quadratic), the profile of the body force $f_b(z)$ is determined from the force balance in Eq. (5). The total amount of extra momentum source within the ABL height, F_b, should be equivalent to the net retarding force due to the friction on the ground, F_{fr},

$$F_b+F_{fr}=\int_0^{H_{ABL}} f_b(z)dz+\rho u_*^2=0. \tag{12}$$

Since the friction velocity u_* can be estimated from the log-law velocity profile, $U(z) = (u_*/\kappa)\log(z/z_0)$, the net body force per unit width required to drive the ABL flow is

$$F_b = -\rho\left[\frac{\kappa U_{ref}}{\log(z_{ref} / z_0)}\right]^2, \tag{13}$$

where U_{ref} is the reference velocity at the reference height z_{ref}. Once the reference velocity and the reference height are set, both the friction velocity and the total amount of required body force can be estimated accordingly.

In the current study, we first performed a precursor simulation with an empty domain whose height is the ABL height. The reference velocity U_{ref} is 20 m/s at the reference height of the ABL height H_{ABL}. The target terrain exposure is the aerodynamic roughness length of z_0 = 0.03 m in full scale corresponding to Exposure C of ASCE 7-22 (2017). These quantities result in the net amount of body force F_b/ρ=0.62 m^2/s^2. This net body force was distributed in the domain using constant and linear profile shapes, respectively, based on target shear stress profiles with linear and quadratic shapes.

In the following simulations, we employ various simulation configurations for the approach flow to investigate their satisfaction of the requirements for structural wind engineering applications, not only in an empty domain simulation but also in a main simulation with a building or topographic features. In the subsequent section, the results are explained with four test cases used in wind engineering simulations.

4. Test cases of approach flow simulations

The CFD approach used in this study employed two steps. The first step is a precursor simulation to obtain the target approach flow characteristics in an empty computational domain (Sec. 4.1). The second step is a main simulation for wind engineering applications using the approach flow profiles from the precursor in a domain extended in the streamwise direction. Three application scenarios were considered using various simulation configurations to investigate the performance of the approach flow for structural wind engineering applications in the main simulations. The three test cases are as follows: (1) approach flow in an extended empty domain (Sec. 4.2), (2) flow around an isolated building (Sec. 4.3), and (3) flow over topographic features (Sec. 4.4). All simulations in the current study are conducted with OpenFOAM v7, open-source CFD package (OpenFOAM, 2019), in 2-D settings with a length scale ratio of 1:1000.

4.1. Test case 1: precursor simulation for approach flow

4.1.1. Computational domain and boundary conditions

To achieve the characteristics of a fully developed boundary layer flow, a precursor simulation was performed until the flow reached an equilibrium between the driving force (i.e., additional momentum source in the governing equation) and the retarding force (wall friction). We considered two different values of the computational domain height (H). The first case is H being equal to the ABL height ($H = H_{ABL}$), and the second one is H being two times the ABL height ($H = 2H_{ABL}$) where H_{ABL} = 1000 m in full scale, as shown in Fig. 1. The length of the domain in the flow direction (L) is H_{ABL} in both cases. As indicated in Table 1, both inlet and outlet boundaries are set to periodic conditions for all variables, in which the flow field can fully develop as in an infinitely long domain along the streamwise direction. Although the current steady RANS study is not capable of predicting the integral length scales of the turbulent flow, it is important to note that the limited domain length and periodic boundary conditions influence the turbulence length scales in precursor simulations, particularly in the case of 3-D unsteady flow (Nandi & Yeo, 2021). A slip condition is specified on the top boundary, while a no-slip condition and wall functions are applied on the bottom boundary.

The computational grids consist of 146 and 158 cells in the vertical direction of the H_{ABL} and $2H_{ABL}$ cases, respectively. The cells in the ABL height are identical for both cases, and the only difference is that the taller domain ($2H_{ABL}$) has additional cells in the upper layer beyond the ABL. The computational grid size is the smallest near the ground and gradually increases toward the top boundary, varying from $0.0015H_{ABL}$ to $0.042H_{ABL}$ in the H_{ABL} case and from $0.0015H_{ABL}$ to $0.141H_{ABL}$ in the $2H_{\mathrm{ABL}}$ case. A constant grid size of $0.05H_{ABL}$ was used in the horizontal direction. Only one cell was used in the lateral direction as a 2-D setting. Figure 1 illustrates the computational domains of the simulations whose domain heights are H_{ABL} and $2H_{ABL}$. The driving forces in both cases were applied up to the height of the ABL (i.e., H_{ABL}) which is indicated as the shaded area in the figure, where the net body force (F_b) from Eq. (13) within the ABL height was distributed on the basis of the target shear stress profile. Considering that the retarding force from the ground friction has negligible effect in the free atmosphere (i.e., in the region above ABL), the body force is also not required in that layer. As a result, the flow characteristics in the free atmosphere are nearly identical to those at the ABL height. Owing to the periodic conditions between the inlet and outlet boundaries, pressure remains constant

throughout the computational domain. The value is identical to the specified reference pressure ($p_{ref} = 0$) at a reference point (e.g., the center of the domain).

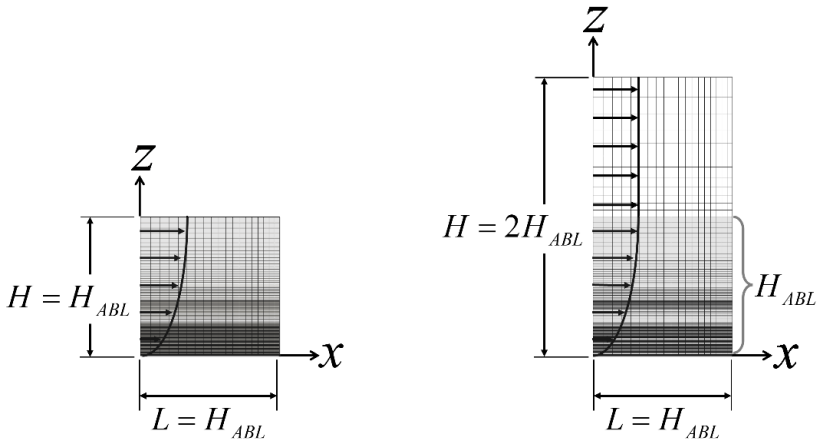

Fig. 1. Computational domains for precursor simulations: (a) $H = H_{ABL}$ and (b) $H = 2H_{ABL}$.

Table 1. Boundary conditions of precursor simulations (OpenFOAM, 2019)

	Inlet	Outlet	Top	Bottom
$\boldsymbol{U}$	periodic	periodic	slip	$\|\boldsymbol{U}\| = 0$
p	periodic	periodic	slip	zeroGradient
k	periodic	periodic	slip	kqRWallFunction
ε	periodic	periodic	slip	epsilonWallFunction
ν_t $(= \mu_t/\rho)$	periodic	periodic	slip	nutkAtmRoughWallFunction, $z_0 = 0.03$ m in FS

4.1.2. Driving mechanism of ABL wind

As discussed in Section 2, the body force term in Eq. (5) can be regarded as a substitute for the pressure gradient that drives the wind flow and determines the shear stress profile in the unidirectional ABL flow. Under the assumption that the pressure field within the ABL is barotropic, pressure varies only by density and its horizontal gradient would be constant throughout the boundary layer region in a computational domain (Cai, et al., 2014). In this case, the body force is constant along the height up to ABL as shown in Fig. 2(a). This constant $f_b(z)$ yields the shear stress profile linearly decreasing from the maximum value at the ground to zero at the ABL height (Richards & Norris, 2019). Since a non-linear shear stress profile has been suggested from observations (e.g., a quadratic form (IHS ESDU, 2001)), this study also included a linearly decreasing body force shown in Fig. 2(b). This produces the shear stress quadratically decreasing over the ABL height. Note that the total amount of body force (i.e., the integration of the force over height), denoted by F_b, is identical for both constant and linear body force cases. This implies that the driving force throughout the ABL height is in equilibrium with the retarding force on the ground. The net driving force (i.e., the body force minus the retarding force) at height generates the flow within the domain and determines the velocity at that height, as

determined by Eq. (13). The profile of the body force in z would influence the profiles of resultant quantities in the ABL height, while the resulting freestream velocity outside the ABL remains unchanged, regardless of the shape. Any appropriate form of shear stress within the ABL can be considered in the wind generation approach. Note that the profiles of a body force and the associated shear stress play an important role on development of the flow field within the ABL height. Since this study does not take into account the Coriolis force in the domain, the body force beyond the ABL height is not applied.

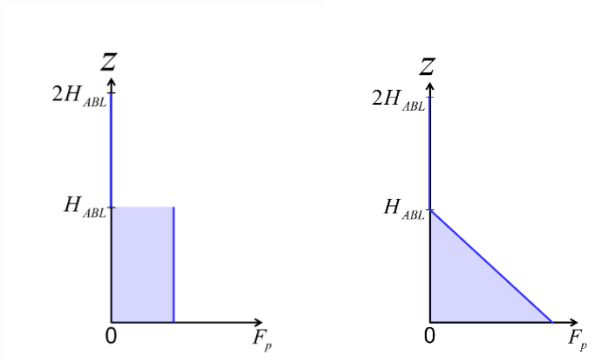

Fig. 2. Shape of momentum source profiles to drive ABL flow in CFD simulations: (a) constant and (b) linear

4.1.3. Results

We present the results of four precursor simulations to investigate the effect of both the height of the computational domain and the shape of the momentum source on ABL flow profiles of streamwise velocity U, turbulent kinetic energy k, the rate of turbulence dissipation ε and the shear stress τ. Figure 3 first presents the U, k, and ε profiles in equilibrium when considering the domain height of H_{ABL} and $2H_{ABL}$ as well as two different body force profiles: constant (solid line) and linear (dashed line). It is observed that, given that the same body force is incorporated, the resultant ABL flow profile compares well between the cases having two different domain heights. All four cases produce very similar profiles for U, k, and ε. However, differences begin to emerge at a height approximately 80% of H_{ABL}, towards the top boundary, due to the boundary effect. In the comparison between the two body force profiles, U does not exhibit differences, except near H_{ABL}. In contrast, the values of k and ε show differences throughout the ABL height.

For quantitative comparison between the two different domain height simulations, we used a relative deviation with respect to the quantities from the simulations with $H = H_{ABL}$. For example, the relative deviation for the streamwise velocity U is determined by

$$e_u(z) = \frac{|U_{2H_{ABL}}(z) - U_{1H_{ABL}}(z)|}{U_{1H_{ABL}}(z)} \times 100[\%]. \tag{14}$$

Figure 4 presents the relative differences of U, k and ε for the cases with constant (solid lines) and linear (dashed lines) momentum source. The maximum discrepancy of all quantities always occurs at the top boundary for all cases regardless of the shape of $f_b(z)$. The maximum relative deviations are 0.98 % for U, 40.2 % for k, and 44.5 % for ε when $f_b(z)$ is constant, while the

deviations are 0.30 % for U, 43.64 % for k, and 48.45 % for ε when a linear body force is applied. Note that such large relative differences at high elevations for k and ε are not necessarily meaningful in structural wind engineering simulations. This is not only due to their occurrence near the ABL height, but also because their values are inherently low.

The next task is to assess whether the body force can successfully generate the desired target shear stress profile. From Eq. (6), the shear stress is the integration of the body force, thus the constant and linear body force profiles $f_b(z)$ theoretically yield linearly and quadratically decreasing shear stress $\tau(z)$ along z, respectively. Figure 5 displays the shear stress profiles of the four precursor simulations, where the black dashed and gray solid lines are the shear stress along the H_{ABL} and $2H_{ABL}$ and domain height, respectively. The dotted lines are the model profile of Eq. (9) with $\gamma = 0$ for the linearly varying shear stress and Eq. (8) for the quadratic one. These results confirm the two key aspects of the proposed approach. Firstly, the shear stress is distributed as we expected. Secondly, shear stress does not present at elevations above the ABL height, where the free atmosphere flow is free from any driving forces and the associated shear stress. In addition, the simulated flow is horizontally homogeneous.

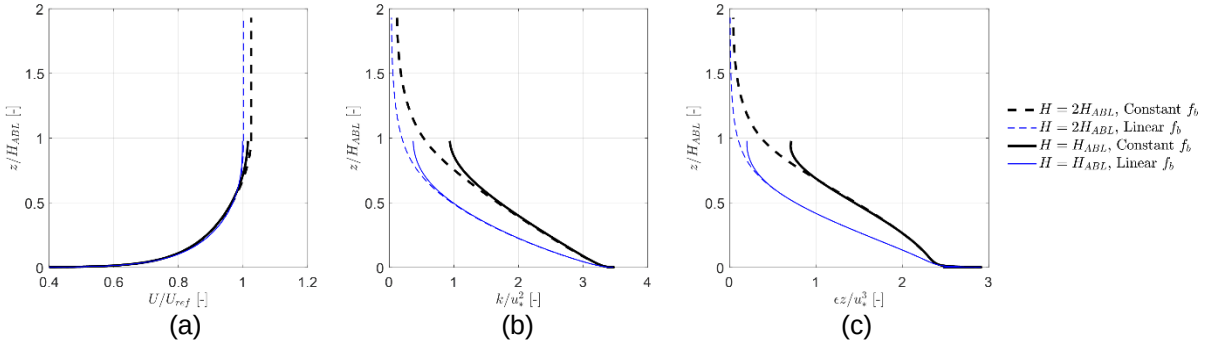

Fig. 3. (a) Velocity U, (b) turbulent kinetic energy k and (c) the rate of turbulent dissipation ε profiles obtained from simulations with constant (black) and linearly decreasing (blue) body forces in two computational domain heights of 1m (solid line) and 2 m (dashed line)

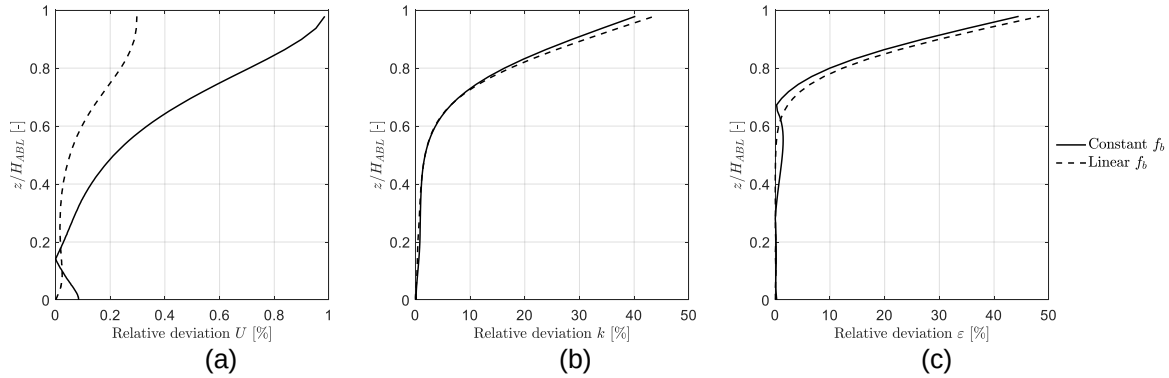

Fig. 4. Profiles of relative deviation between two different domain heights with incorporating constant body force (solid) and linearly decreasing (dashed) body force: (a)velocity, (b)TKE and (c)dissipation rate

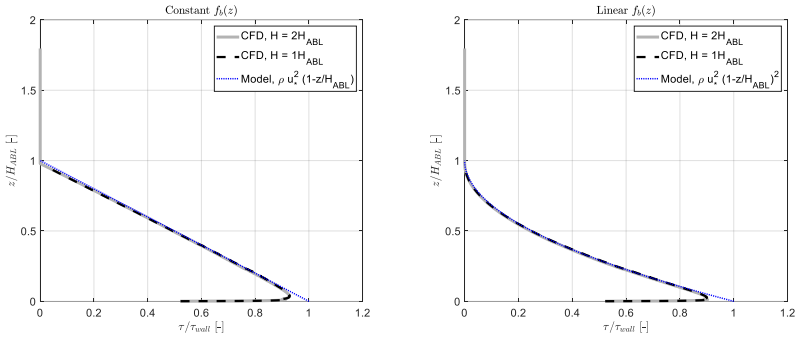

(a) (b)

Fig. 5. Resulting shear stress profiles of precursor simulations using (a) constant and (b) linear body force

4.2. Test case 2: approach flow simulation in an extended empty domain

4.2.1. Computational domain and boundary conditions

Once a target approach flow is obtained from a precursor simulation (Sec. 4.1), this approach flow is then applied in a main simulation that includes, e.g., a building of interest for structural engineering applications. This two-stage simulation approach is valid if the approach flow in the main simulation remains consistent with the flow generated in the precursor. To address this question, we conducted an investigation of the flow in a main simulation with a horizontally extended empty domain (the streamwise domain size = $10H_{ABL}$). For a successful two-stage simulation, it is essential that the flow in the main simulation exhibits characteristics of horizontal homogeneity and a zero-pressure gradient along the wind direction, consistent with the flow from the precursor simulation. Also, it is important that the U, k and ε profiles obtained from the precursor simulations remain unchanged or vary only negligibly in the subsequent main simulation. To achieve the goal, we carried out an analysis of the main simulation setups, using the different body force profiles and domain heights described in the previous section. The computational domains in the main simulation were constructed by replicating the precursor domains 10 times in the x (along-wind) direction as shown in Fig. 6. In the figure, the shaded area of the domain indicates the area to which the body force was applied. One important aspect to consider in the main simulation is the inclusion of the body force within the domain. Many numerical studies using a body-force-driven approach flow have only mapped the precursor results at the inlet boundary of the main simulation, without incorporating the driving body force throughout the domain.

In contrast to the precursor simulations using periodic boundary condition at the inlet and outlet boundary, the main simulations with the horizontally extended domain map the U, k and ε profiles obtained from the precursor to the inlet and set zero-gradient condition at the outlet. As a result, the main simulations are able to maintain the fully developed flow from the precursor in the area prior to any disturbance by obstacles, such as buildings, within the domain. The boundary conditions for the top and the bottom boundaries remain unchanged from the precursor simulations as outlined in Table 2. For accurate estimation of pressure field, a reference pressure was set to 0 at $z=H_{ABL}$ of the inlet boundary.

Table 2. Boundary conditions of simulations for elongated domain

	Inlet	Outlet	Top	Bottom
$\boldsymbol{U}$	fixedValue (from precursor)	zeroGradient	slip	$\|\boldsymbol{U}\|=0$
p	zeroGradient	zeroGradient	slip	zeroGradient
k	fixedValue (from precursor)	zeroGradient	slip	kqRWallFunction
ε	zeroGradient	zeroGradient	slip	epsilonWallFunction
ν_t	zeroGradient	zeroGradient	slip	nutkAtmRoughWallFunction, z_0 = 0.03 m in FS

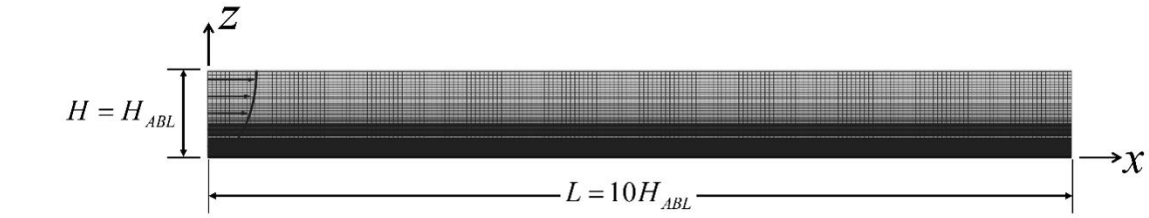

(a)

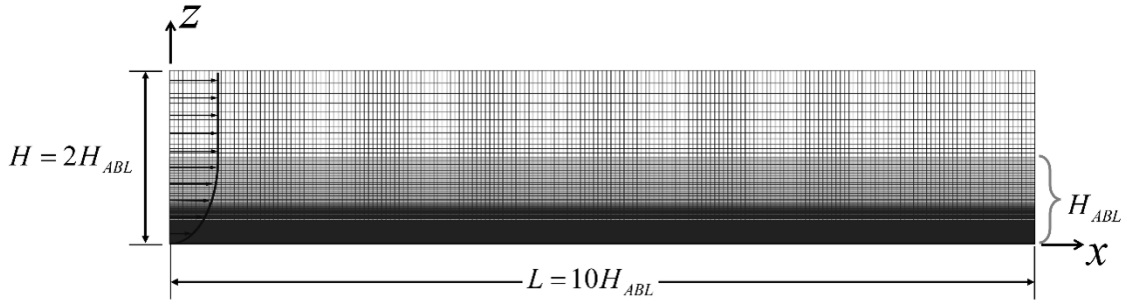

(b)

Fig. 6. Computational domains for the main simulation: horizontally-extended empty domain

4.2.2. Results

We examined whether the flow profiles obtained from a precursor simulation would maintain horizontal homogeneity and zero streamwise pressure gradient in a main simulation that utilized the longer computational domain of L = 10 H_{ABL} (Fig. 6).
Figure 7 displays the changes in the U, k, and ε profiles as they progress along the computational domain of $H = H_{ABL}$. The plots of (a) and (b) in the figure represent the cases with and without

the inclusion of the constant body force, respectively. Each plot consists of 6 graphs, with the top row showing the profiles at three different locations (i.e., at the inlet, in the middle of the domain length and at the outlet), and the bottom row displaying relative deviations of the profiles at the three locations with respect to those specified at the inlet. It is observed that the flow in the main simulations successfully maintain the U, k, and ε profiles generated from the precursor simulation throughout the entire empty domain, regardless of the presence of the body force $f_b(z)$. The maximum discrepancy of U, k, and ε between the inlet and the outlet is 0.04 %, 0.94 % and 1.27 % when the body force is applied, and 0.04 %, 0.90 % and 1.14 % without the force, respectively. Although the relative change is greater for k and ε than that of U, it is noteworthy that the actual change could be negligible due to their relatively small absolute values.

Figure 8 shows the changes in U, k, and ε profiles along the streamwise direction in the $H=2H_{\mathrm{ABL}}$ simulations. Compared with the $H = H_{\mathrm{ABL}}$ simulations (Fig. 7), all of the quantities generally exhibit a reduced degree of horizontal homogeneity in the case without the constant body force. The main simulation without inclusion of the body force experiences greater variation of flow conditions as it goes downstream. The maximum relative variations of U, k, and ε from the inlet to the outlet are 1.05%, 4.53% and 7.06%, respectively. However, the main simulation with the body force exhibits reduced variation along the streamwise direction, with values of 0.12 %, 0.40 % and 1.33 % for the maximum relative variation of U, k, and ε, respectively, from the inlet to the outlet.

Figures 9 and 10 display the main simulation results with and without inclusion of the linearly varying body force, respectively. The results display a trend that is similar to those obtained when using the constant force (Fig. 7 and Fig. 8). Inclusion of the body force successfully maintains the U, k, and ε profiles obtained from the precursor simulation throughout the extended computational domain, regardless of domain height relative to H_{ABL}.

In summary, the approach flow in the main simulation remains horizontally homogeneous for the case where $H = H_{\mathrm{ABL}}$, regardless of whether the body force is present or not. This horizontal homogeneity with or without the body force is particularly evident when the body force profile is constant, while for the linear body force profile, some deterioration of the horizontal homogeneity is noticeable when the body force is omitted. However, when the main simulation does not incorporate the body force in the domain with $H = 2H_{\mathrm{ABL}}$, the horizontal homogeneity gradually deteriorates along the streamwise direction. This deterioration is more pronounced in the k and ε profiles than in the U profile. The maximum relative change for k and ε along the streamwise distance of $10H_{ABL}$ is approximately 15 %, which cannot be ignored in simulations for structural engineering applications. In contrast, when the body force is present, the main simulation is able to maintain the horizontally homogeneous characteristics of the approach flow in the along-wind direction with a maximum relative change of approximately 2 % for k and ε.

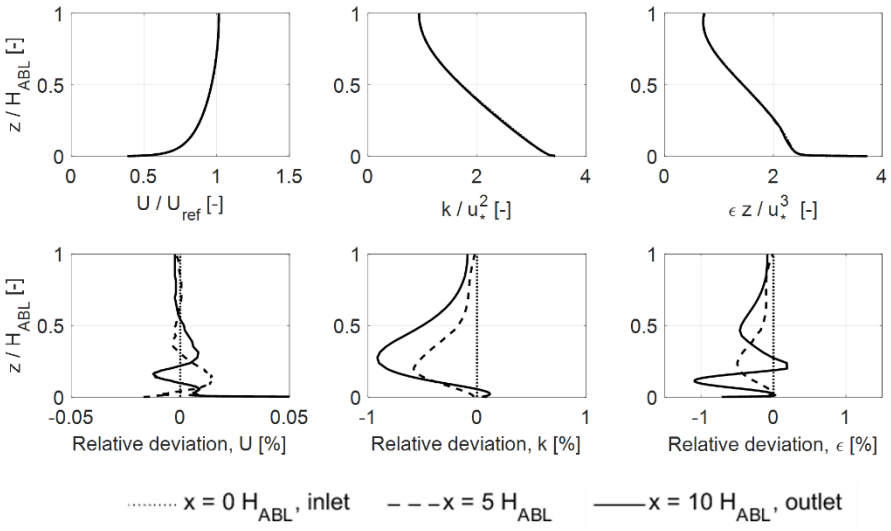

(a) With constant body force

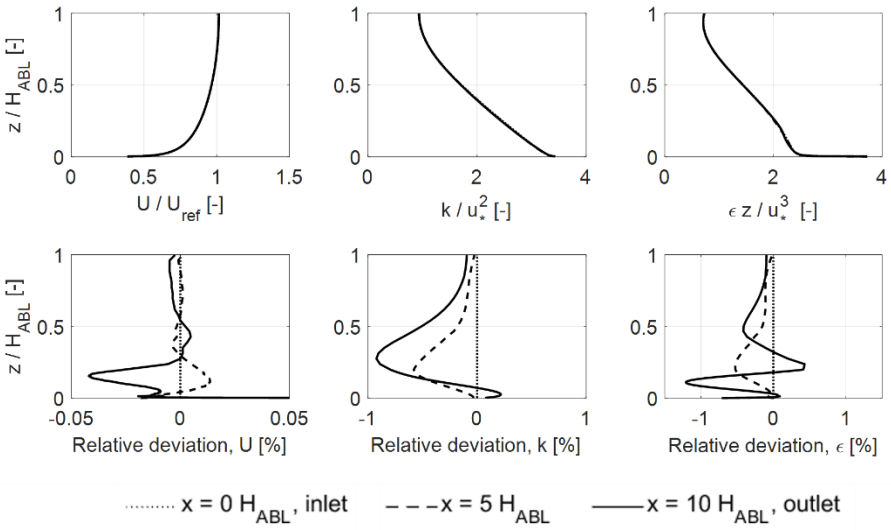

(b) Without constant body force

Fig. 7. *U, k*, and *ε* profiles at three locations (inlet, center and outlet) and relative errors with and without incorporating constant momentum source in simulations with domain height of H_{ABL}

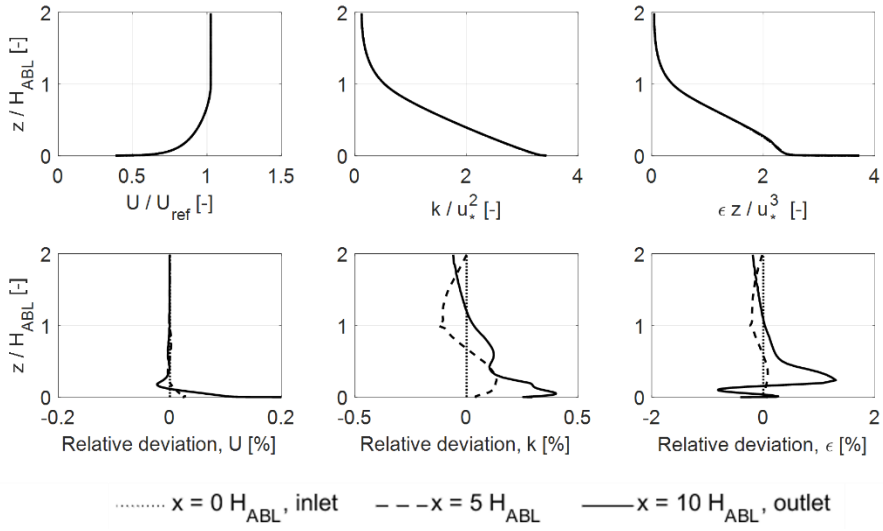

(a) With constant body force

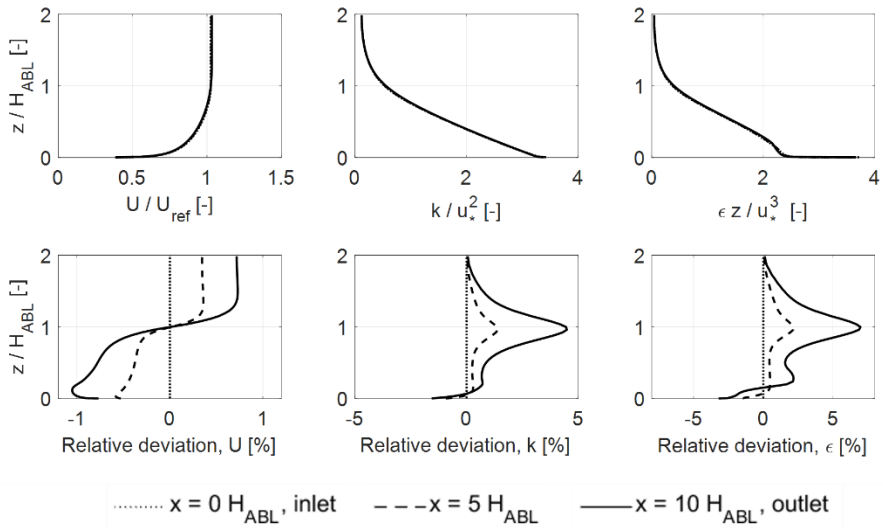

(b) Without constant body force

Fig. 8. *U, k*, and *ε* profiles at three different locations (inlet, center and outlet) and relative errors with and without incorporating constant body force in main simulations with domain height of $2H_{ABL}$

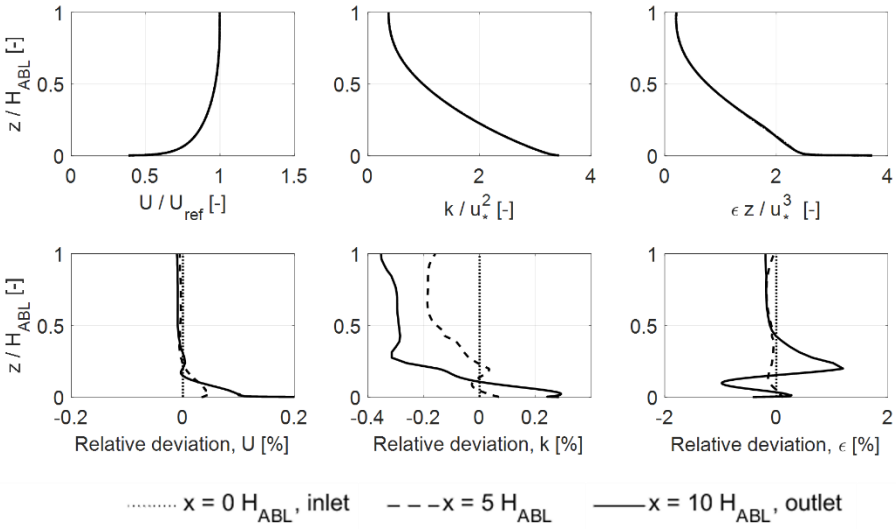

(a) With linearly varying body force

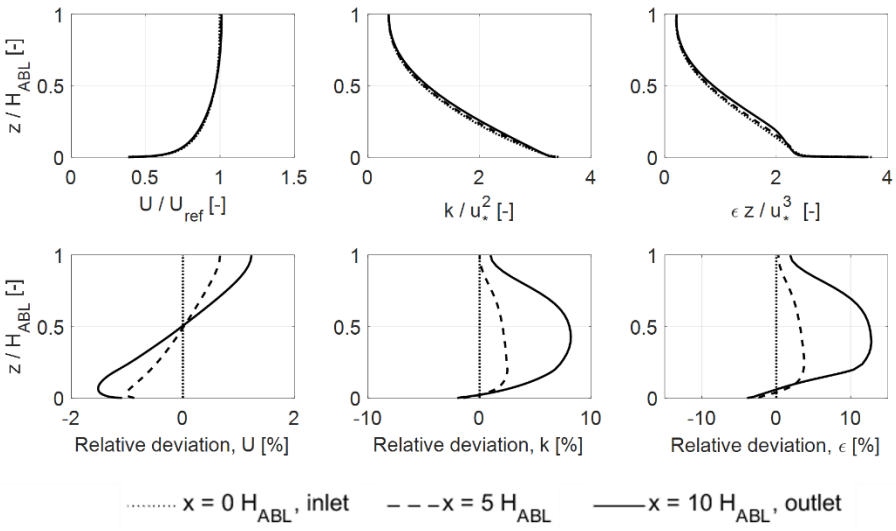

(b) Without linearly varying body force

Fig. 9. *U*, *k*, and *ε* profiles at three different locations (inlet, center and outlet) and relative errors with and without incorporating linearly varying body force in main simulations with domain height of H_{ABL}

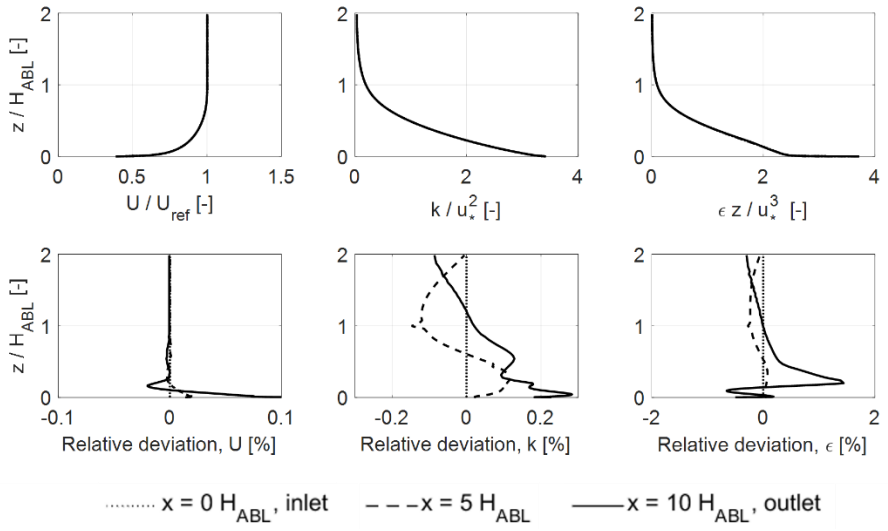

(a) With linearly varying body force

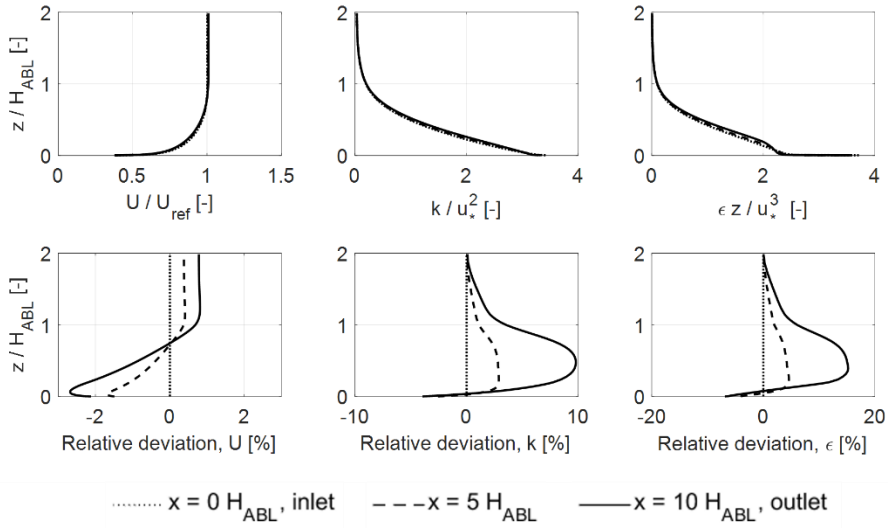

(b) Without linearly varying body force

Fig. 10. *U*, *k*, and *ε* profiles at three different locations (inlet, center and outlet) and relative errors with and without incorporating linearly varying body force in main simulations with domain height of $2H_{ABL}$

Next, the pressure distribution throughout the computational domain was analyzed to confirm whether the zero streamwise pressure gradient condition is ensured with our proposed approach. Although a previous study noted a change in horizontal pressure when the body force was not included in the main simulation (Cindori, et al., 2020), the cause and impact of this change have not been fully investigated. In this study, we conducted a thorough examination of how the presence or absence of the body force in the main simulations affects the pressure field within the domain. Figure 11 displays the pressure contours of all eight main simulations of the empty domain. Note that the pressure is constant along the *z* direction in all cases. Regardless of the shape of the body force, either constant or linear, zero pressure gradient is achieved if the body force is present in the simulation. However, when the body force is absent in the main simulation, a streamwise pressure gradient is developed in the along-wind direction. This result indicates that the ideal zero pressure gradient condition can be guaranteed in the domain only if the body force is included in the main simulation. This observation can be explained with Eq. (5). If the body force, which is the original driving mechanism of the ABL flow in the precursor simulation, is not included in the main simulation, the streamwise pressure gradient field is automatically generated within the domain to substitute the missing driving force and to keep the U, k, and ε profiles homogeneous along the streamwise direction. This explanation can be verified by examining the pressure along a horizontal line at the ABL height in Fig. 12. The figure presents the pressure profile normalized by the total amount of body force, where the two subfigures correspond to the use of different domain heights of H_{ABL} and $2H_{ABL}$. For both domain heights, the pressure gradient is zero if the body force is incorporated within the ABL height in the main simulation (blue dotted lines), but the pressure decreases when the body force is absent (black lines). The normalized pressure shows the slope of 1 with the domain height (H) being exactly the ABL height, and the slope decreases to approximately 0.5 if the domain height is doubled while the body force is applied up to the ABL height. This indicates that the automatically generated pressure gradient is equivalent to the body force per unit length, i.e., $(\Delta p / \Delta x)H \approx F_b$. It is important to note that the driving force of F_b is applied up to the ABL height (H_{ABL}) in the precursor simulation, while in the main simulation without the applied body force, it generates a constant pressure gradient ($\Delta p/\Delta x$) being distributed from the ground to the domain height of $H=2H_{ABL}$. Thus, in comparison with the case where $H = H_{ABL}$, the pressure gradient is reduced by half when $H = 2H_{ABL}$, as shown in Fig. 12. This implies that the body force in the precursor simulation is consistent with the pressure gradient generated in the main simulation only when a constant body force is used and $H = H_{ABL}$. In a case of the linearly varying body force, the equivalent pressure gradient vertical profile should also vary linearly along the height. However, as previously mentioned, the pressure at any given streamwise location does not change along the vertical direction. As a result, the main simulation without the linearly varying body force cannot be consistent with one that includes the body force. Therefore, to achieve an approach flow in the main simulation that is both horizontally homogeneous and has a zero streamwise pressure gradient, it would be ideal to apply a constant body force up to the ABL height in both precursor and main simulations, regardless of the domain height. It is also worth noting that for wind engineering applications that focus solely on flow field, either a constant or a linearly varying body force could be used in both the precursor and main simulations.

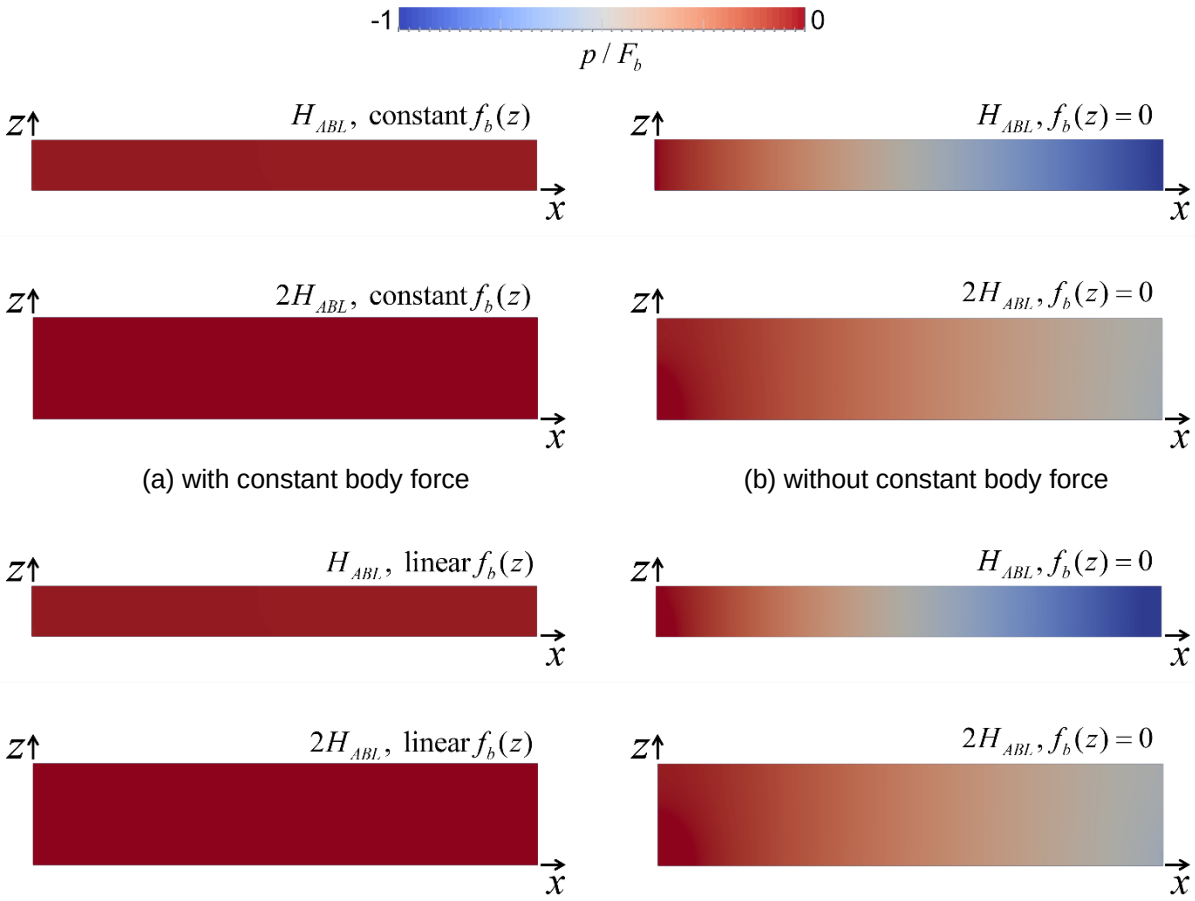

(a) with constant body force

(b) without constant body force

(c) with linearly varying body force

(d) without linearly varying body force

Fig. 11. Pressure contours of the main simulations with an empty computational domain when incorporating (a,b) with/without constant body force and (c,d) with/without linearly varying body force

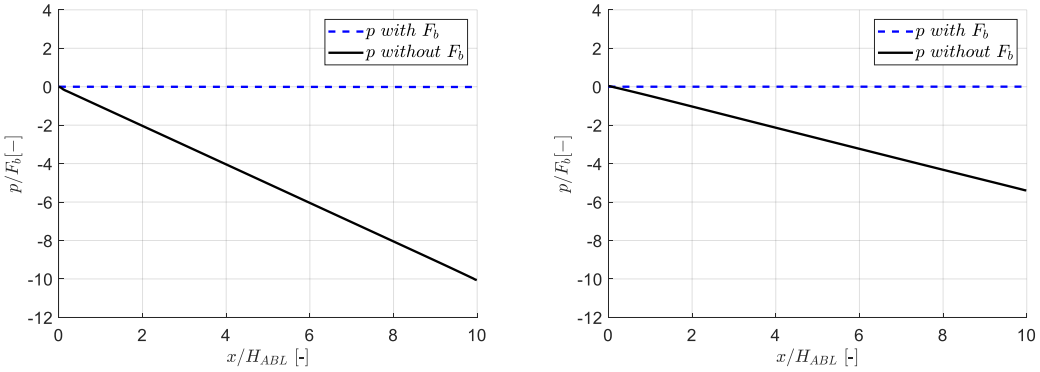

(a) $H = H_{ABL}$

(b) $H = 2H_{ABL}$

Fig. 12. Pressure profile along the horizontal line crossing the computational domain at $z = H_{ABL}$

4.3. Test case 3: Simulation of ABL flow over an isolated building

The previous section investigated the effects of simulation settings for flow generation on horizontal homogeneity of flow, particularly for horizontal pressure gradient, in an empty domain simulation. This section examines their effects on the flow field around and pressure on an isolated structure located in the computational domain. Firstly, we investigated the effect of the constant body force on flow fields in the main simulation, with the domain height being either equal to or taller than the ABL height ($H = H_{ABL}$ or $H = 2H_{ABL}$). Secondly, we further increased the domain height to $4H_{ABL}$ and $8H_{ABL}$ to understand effects of blockage ratio on aerodynamic pressure on the structure in the main simulation with the presence of the body force.

4.3.1. Simulation setup: model description, domain and boundary conditions

Figure 13 provides an overview of computational domains with examples of (a) H_{ABL} and (b) $2H_{\mathrm{ABL}}$, as well as (c) the computational grid around the building. As illustrated in the figure, an isolated building is located at $4H_{\mathrm{ABL}}$ downstream from the inlet, where the building has both height and length of $H_b = 0.025H_{\mathrm{ABL}}$. This leads to the blockage ratio of 2.5 % and 1.25 % for the domain sizes (H) of H_{ABL} and $2H_{\mathrm{ABL}}$, respectively, in the 2-D simulation. Each edge of the building has 20 cells to ensure that the simulations can accurately capture important flow phenomena around the bluff-body geometry, including separation of flow from the sharp leading edge and re-circulation behind the leeward wall. Computational grids with the domain height of $4H_{ABL}$ and $8H_{ABL}$ are created for the investigation of blockage effect on flow quantities in the vicinity of the target building. Boundary conditions are summarized in Table 3.

Table 3. Boundary conditions for the main simulation with an isolated building

	Inlet	Outlet	Top	Bottom	Building surface
$\boldsymbol{U}$	fixedValue (from precursor)	zeroGradient	slip	$\lvert\boldsymbol{U}\rvert=0$	$\lvert\boldsymbol{U}\rvert=0$
P	zeroGradient	zeroGradient	slip	zeroGradient	zeroGradient
K	fixedValue (from precursor)	zeroGradient	slip	kqRWallFunction	kqRWallFunction
ε	zeroGradient	zeroGradient	slip	epsilonWallFunction	epsilonWallFunction
ν_t	zeroGradient	zeroGradient	slip	nutkAtmRoughWallFunction, z_0=0.03 m in FS	nutkWallFunction

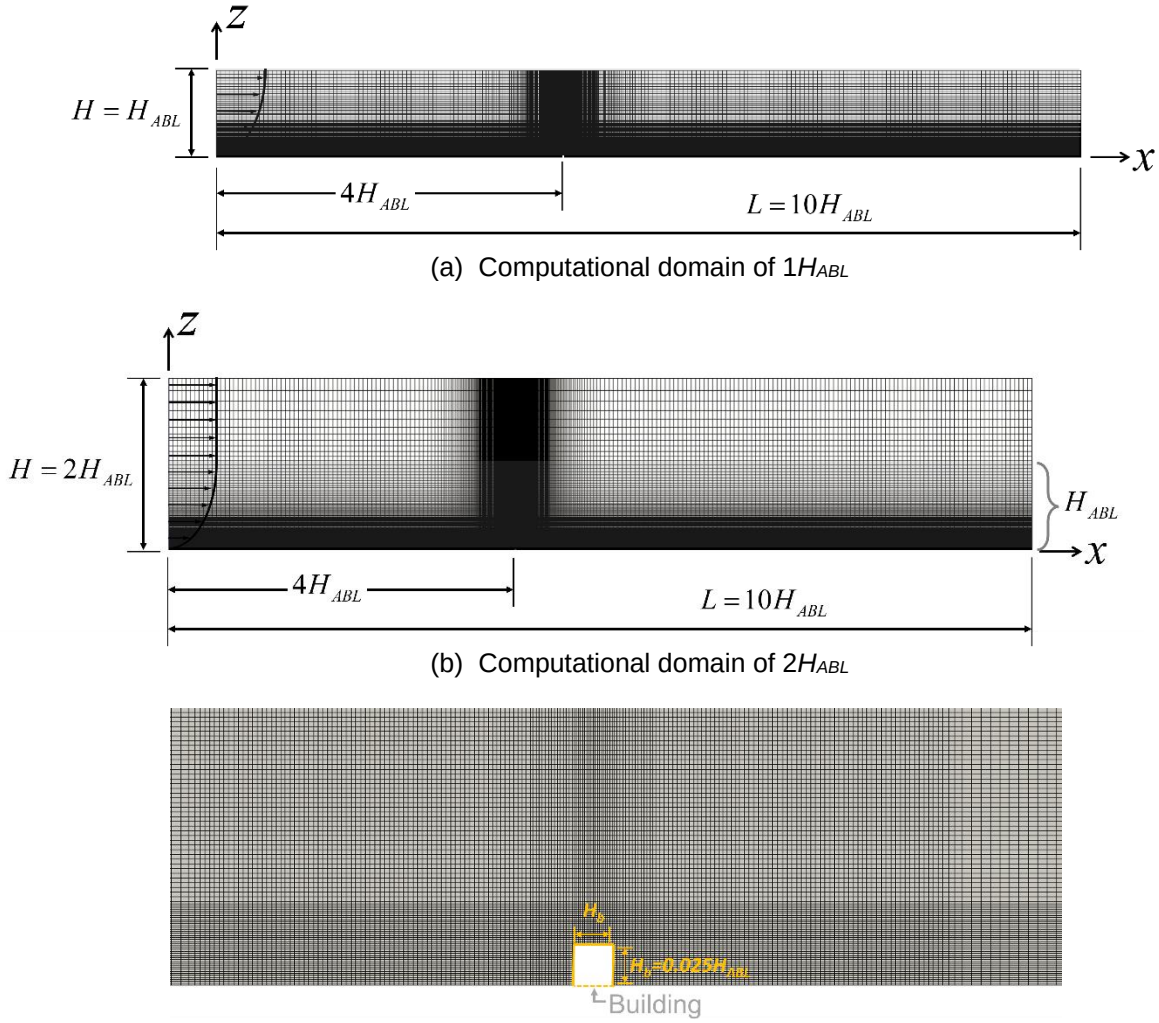

(a) Computational domain of 1H_{ABL}

(b) Computational domain of 2H_{ABL}

(c) Mesh distribution around the building geometry

Fig. 13. Schematics of computational domain of (a) H_{ABL} and (b) 2H_{ABL}, and (c) the computational grid around the test case building

4.3.2. Results

This section focuses on the flow fields around, and the pressure on, a building structure, focusing on the presence of a body force and the effect of a vertically extended domain. Figure 14 shows the velocity and turbulence kinetic energy fields around the building in the four simulation cases depending on existence of constant body force and vertical extension of the domain: (a,e) constant body force and $H = H_{ABL}$, (b,f) no body force and $H = H_{ABL}$, (c,g) constant body force and $H = 2H_{ABL}$, and (d,h) no body force and $H = 2H_{ABL}$. The velocity and TKE fields appear visually similar across all cases, regardless of changes in simulation settings. To investigate this further, we compared their vertical profiles, as shown in Fig. 15. The figures display the non-

dimensional U and k profiles around the building at every H_b interval and the maximum discrepancy between the cases are 0.011 for U/U_{ref} in the wake region and 0.019 for k/u_*^2 at the leeward corner of the building, respectively. This indicates that the modifications in simulation settings have a minute impact (< 2 %) on the velocity and TKE fields.

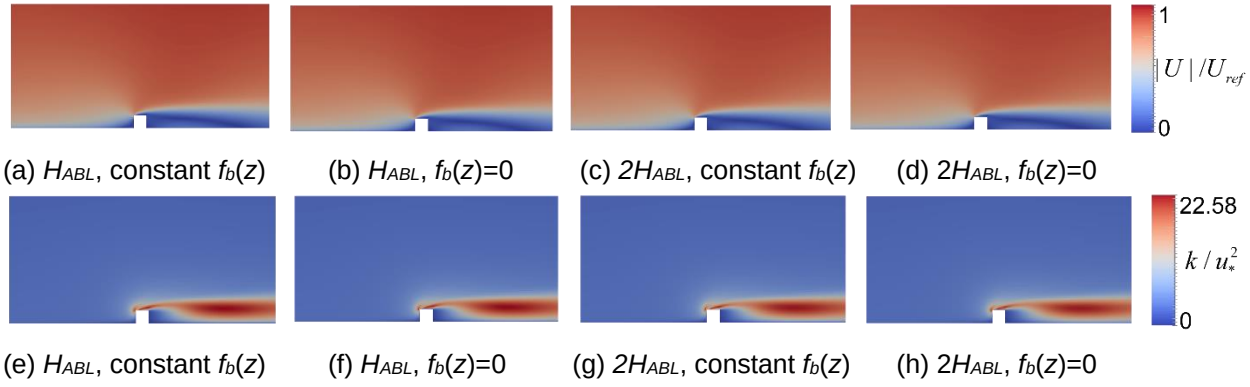

(a) H_{ABL}, constant $f_b(z)$ (b) H_{ABL}, $f_b(z)$=0 (c) $2H_{ABL}$, constant $f_b(z)$ (d) $2H_{ABL}$, $f_b(z)$=0

(e) H_{ABL}, constant $f_b(z)$ (f) H_{ABL}, $f_b(z)$=0 (g) $2H_{ABL}$, constant $f_b(z)$ (h) $2H_{ABL}$, $f_b(z)$=0

Fig. 14. Contours of nondimensional velocity (top) and turbulence kinetic energy (bottom) around the building in main simulations with different settings for the approach flow.

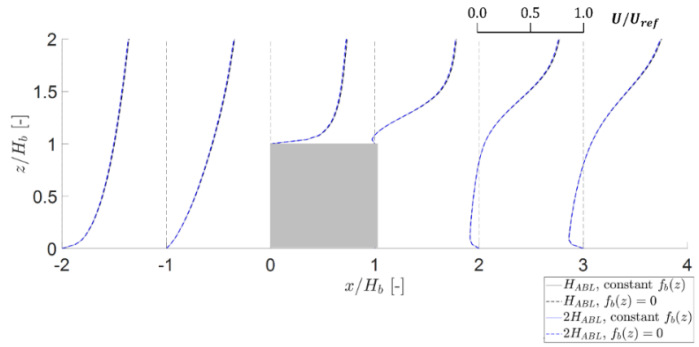

(a) U/U_{ref}

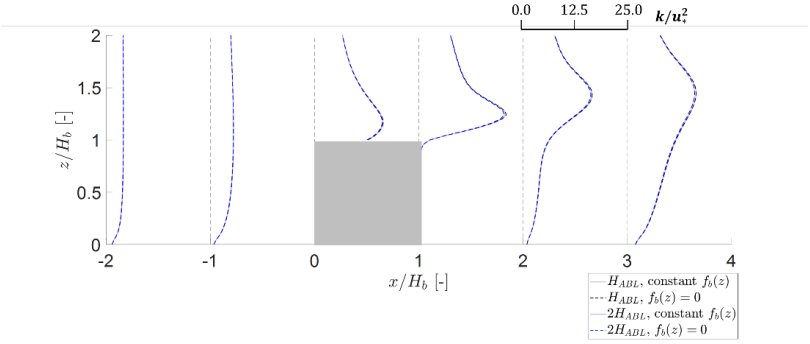

(b) k/u_*^2

Fig. 15. Vertical profiles of nondimensional velocity and TKE around the building in simulations with different settings for the approach flow.

Figure 16 compares the pressure distribution on the ground surface and the building surface, where the pressure coefficient (C_p) is defined as

$$C_p = \frac{p - p_{ref}}{\frac{1}{2}\rho U_{ref,geom}^2}, \tag{15}$$

where p_{ref} is the reference pressure, which is 0 sampled at the ABL height (H_{ABL}) of the inlet, $U_{ref,geom}$ is the reference velocity at the height of the building (H_b) at the inflow boundary, and ρ is the air density. As shown in the figure, the presence of the body force noticeably affects pressure field in the domain. In the case of $H = H_{ABL}$ (Fig. 16(a)) with absence of the body force, the difference in pressure coefficient linearly increases from zero at the inlet to 0.06 at the outlet. This gap is attributed to the presence of the pressure gradient automatically generated in the simulation without the body force. As shown in the right plot of Fig. 16(a), the slope of $(\Delta p/\Delta x)/F_b$ is unity where Δp is the difference of pressure between the two simulations (i.e., the pressure in the simulation with the body force minus the pressure in the simulation without it). It confirms that a constant gradient pressure field automatically builds up in the computational domain in the simulation without the body force and perfectly replaces the missing F_b to develop a consistent flow field. This closely aligns with the observations from the empty simulations in the previous section.
In the case of $H = 2H_{ABL}$ (in Fig. 16(b)), the difference of C_p and the slope of $(\Delta p/\Delta x)/F_b$ between the two simulations with/without the body force are reduced by half in comparison with those in H=H_{ABL}. This result is also consistent with observations in the empty domain simulations as mentioned in Section 4.2.

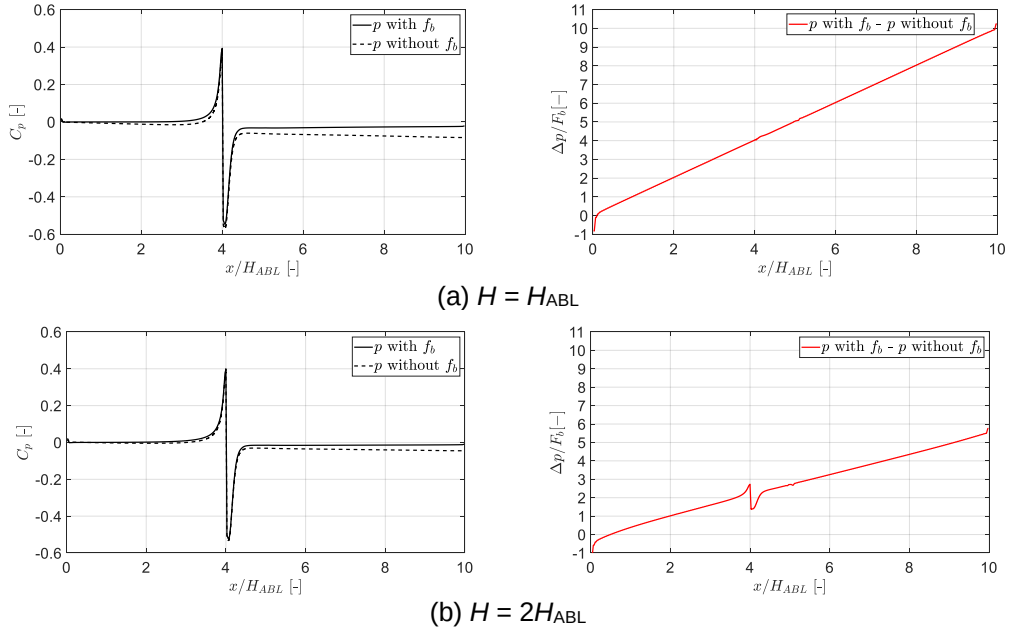

(a) $H = H_{ABL}$

(b) $H = 2H_{ABL}$

Fig. 16. Pressure distribution on the bottom (ground) and building surface of two different cases (a) $H = H_{ABL}$ and (b) $H = 2H_{ABL}$: C_p of two simulations with and without momentum force (left), and the pressure difference between two simulations normalized by total amount of the body force (right).

Figure 17 shows the pressure distribution on the building facades along its edges. The trend of predictions is identical to those observed on the bottom boundary as shown in Fig. 16. When the domain height is exactly the ABL height ($H = H_{ABL}$), the difference in the predicted pressure between the two simulations with/with the body force is $\Delta p/F_p = 4$ as expected since the building is located at $4H_{ABL}$ downstream from the inlet. Unlike this case, when $H = 2H_{ABL}$, the pressure difference is not constant along the edge of the building because of the generated pressure gradient distributed in the domain height of $2H_{ABL}$ as previously described. Although the pressure in a simulation without body force can be corrected if the horizontal pressure gradient information is available, a simulation with the constant body force would be ideal for structural wind engineering applications to produce flow field with no horizontal streamwise pressure gradient in the computational domain. Therefore, further investigation into the effect of blockage ratio was focused on the simulations that incorporated the body force. Figure 18 displays distribution of the relative deviation (Eq. (16)) in velocity magnitude ($|\boldsymbol{U}|$) and turbulence kinetic energy (k) as well as difference in pressure coefficient (C_p) between two simulations with the highest and lowest blockage ratio of 2.5 % and 0.3125 %. Note that the simulation results of the lowest blockage case are used as a reference for the calculation of the relative deviation, for example, $e_k=|k_{2.5\%}-k_{0.3125\%}|/k_{0.3125\%}$. For the pressure, the absolute difference is used instead of the relative deviation because the pressure field far from the building geometry is close to zero which results in tremendously high values when calculating relative deviation. In each contour, higher absolute value at a location indicates a greater blockage effect on the corresponding field variable. Overall, the impact of blockage is greater near the building, with the velocity magnitude and TKE showing maximum deviations of approximately 3 % in each field variable. For the pressure, ΔC_p is low on the windward side of the model where the flow field is not significantly affected by the building, but starts to increase where the flow is obstructed by the building model at $x = H_b$ with a maximum discrepancy of $0.06C_p$.

If the computational domain increases in its height, the blockage effect more evenly spreads out up to the top of the domain, so the overall velocity increase becomes smaller. Therefore, the domain should be tall enough not to have unwanted blockage effects on a structure. Figure 19 presents the convergence of nondimensional velocity, TKE and pressure as a function of the blockage ratio from 2.5 % to 0.3125 %. This change is achieved by increasing the height of computational domain from H_{ABL} to $8H_{ABL}$. The quantities were sampled at the four locations (P_1, P_2, P_3 and P_4) that are either horizontally or vertically apart from the corners of the building geometry by H_b., as shown in Fig. 19. The points P_1 to P_4 are located in the area where the flow field is significantly affected by the building geometry. First of all, the sensitivity of U, k and p to the blockage ratio vary by the sampling locations as well as each of the field variables. The velocity at P_4 changes by only 0.11 % when the blockage ratio is reduced from 2.5 % to 0.3125 %, while the variation of U at P_1 is 1.19 % for the same change in the blockage ratio. Compared to U, the change in TKE is the greatest at P_4 among the four sampling points. The average precent change of the four points is 0.9 % for U, 0.76 % for k and 7.08 % for p. The percent deviation of the pressure is one order of magnitude greater than the other two quantities. This confirms that pressure is more sensitivity to blockage ratio than velocity or its fluctuations. Since the pressure on building surfaces is of primary interest to structural engineers, it was sampled at the center of the windward, top and leeward facades, denoted by P_a, P_b and P_c, respectively, as shown in Fig. 20. The differences in pressures between the lowest and highest blockage are 2.45 %, 4.75 % and 6.04 %, respectively, for P_a, P_b and P_c. Their mean value is 4.41 %, which is lower than the change in pressure at P_1 through P_4 shown in Fig. 19(c) but still greater than the

change in velocity and TKE at the same points. Figure 21 shows the relative deviation of pressure coefficient on the building façade between the highest and lowest blockage cases of 2.5 % and 0.3125 %. The results agree with the pointwise comparison made with Fig. 20, but displays greater deviation of 17% near the top of the windward façade as the pressure itself is lower than the other location on the same facade. Excluding the outlier, the mean deviation is approximately 4.72 %. Figure 22 presents the change in building drag coefficient with respect to the blockage ratio, where the drag coefficient is defined as $C_d = F_{drag} / (0.5\ \rho\ U_{ref,geom}^2\ A_{building})$ with the drag force induced by the building F_{drag} and the frontal area of the building $A_{building}$. In contrast to C_p, which is estimated with pressure sampled at a specific point, C_d is calculated with using the force distribution on building facades and presents less blockage effect by averaging out local variation. The blockage effect can be approximately evaluated with an empirical relation, and the evaluated blockage corrections are 4 % and 0.5 % for the blockage ratios of 2.5 % and 0.3125%, respectively (Melbourne, 1982; Simiu & Yeo, 2019). Given that relatively low influence of blockage ratio on the velocity and turbulence kinetic energy, a computational domain with a low height may be employed for environmental wind simulations. This can reduce computational cost, depending on the acceptability of the blockage effects on simulation results. However, when the accurate estimate of wind-induced pressure on a structure is important from a structural engineering perspective, the blockage must be lowered enough to avoid deterioration of computational solutions due to the blockage effect.

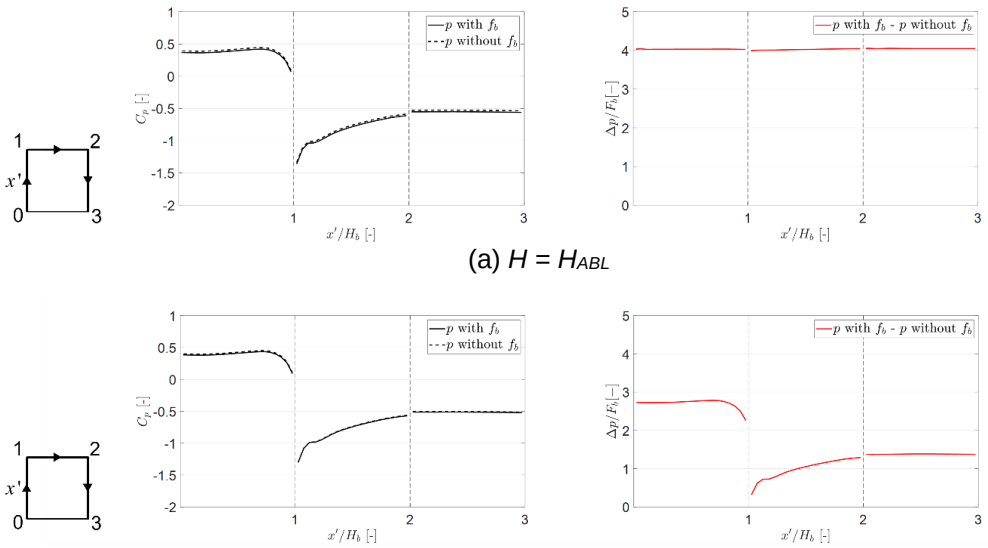

(a) $H = H_{ABL}$

(b) $H = 2H_{ABL}$

Fig. 17. Pressure distribution on the building facades of two different cases (a) $H = H_{ABL}$ and (b) $H = 2H_{ABL}$; C_p of two simulations with and without momentum force (left), and the pressure difference normalized by total amount of the extra momentum force (right).

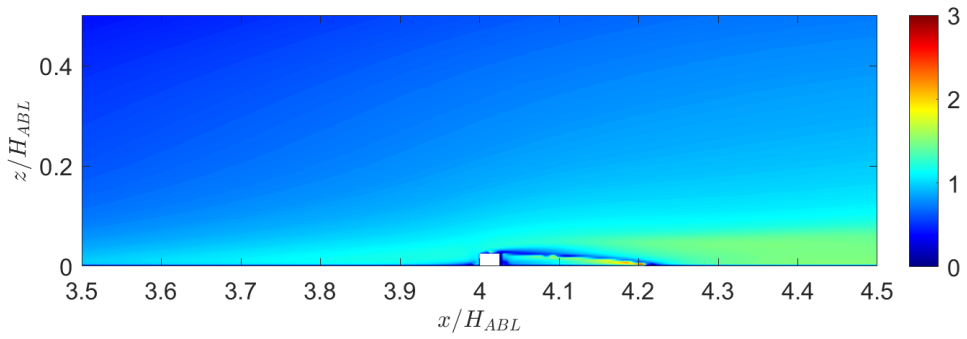

(a) Relative deviation of velocity magnitude [%]

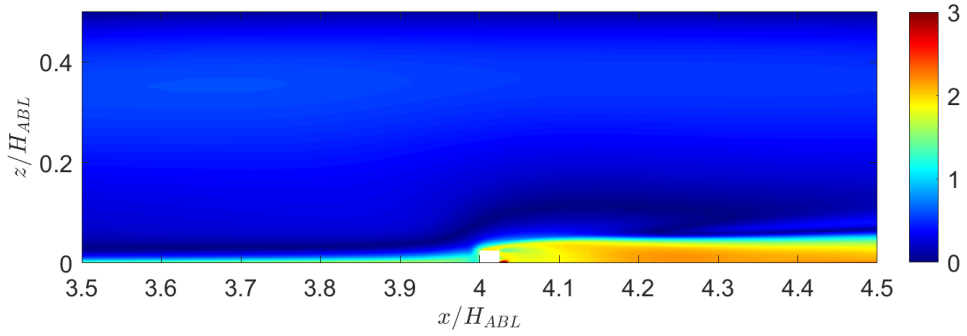

(a) Relative deviation of TKE [%]

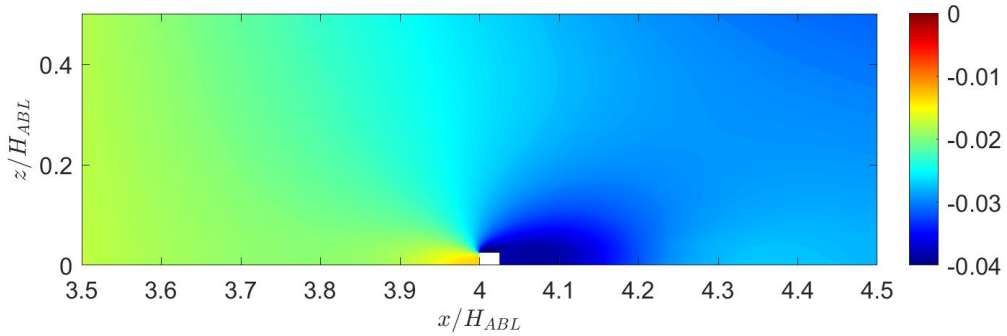

(a) Difference in pressure coefficient [-]

Fig. 18. Relative deviation in (a) velocity magnitude and (b) TKE; and (c) difference in pressure coefficient; between the two simulations with blockage ratio of 2.5 % and 0.3125 % using the lowest blockage case as reference for the relative deviation.

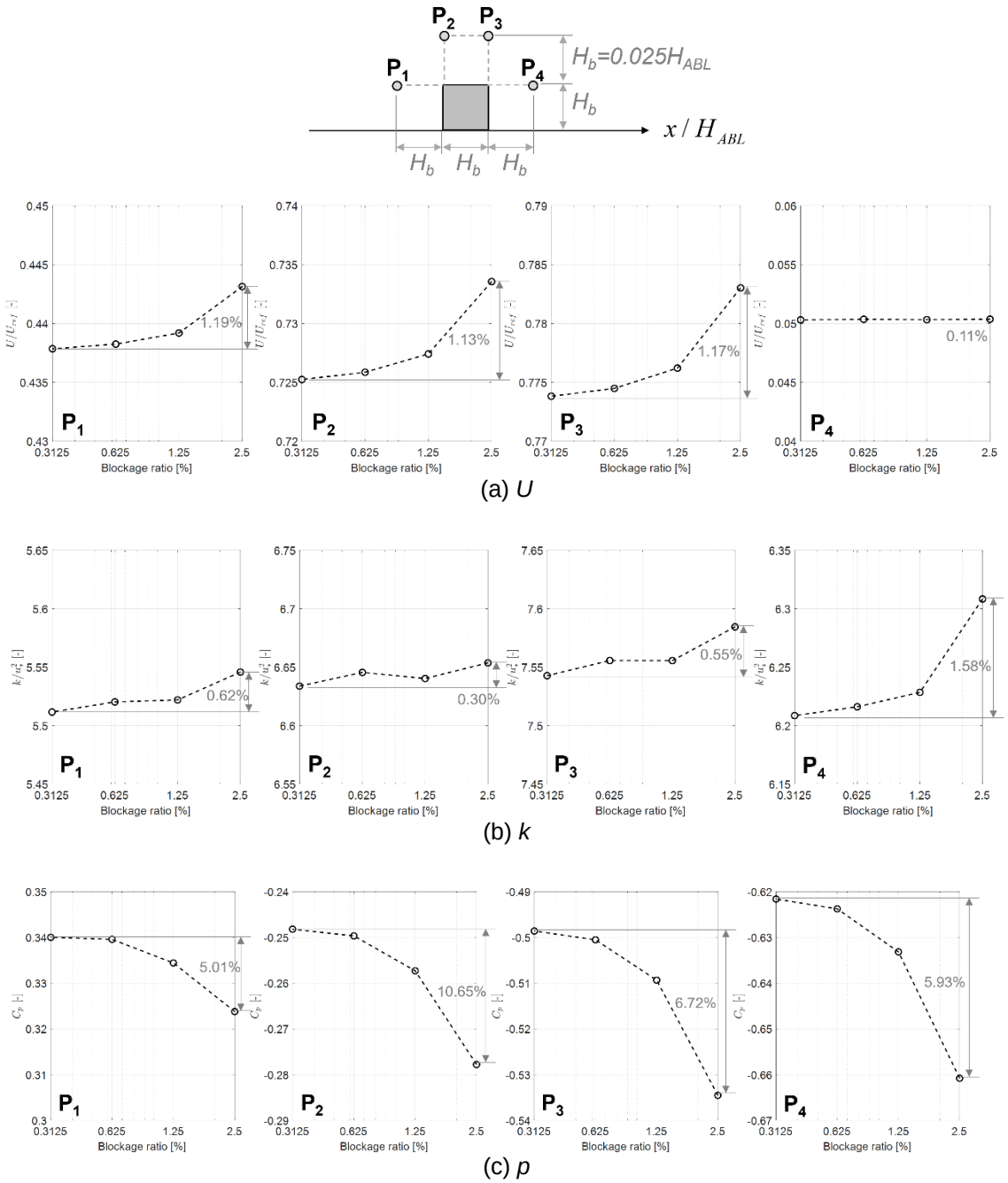

Fig. 19. Change of nondimensional (a) velocity, (b) TKE and (c) pressure at the four locations around the building geometry with respect to blockage ratio.

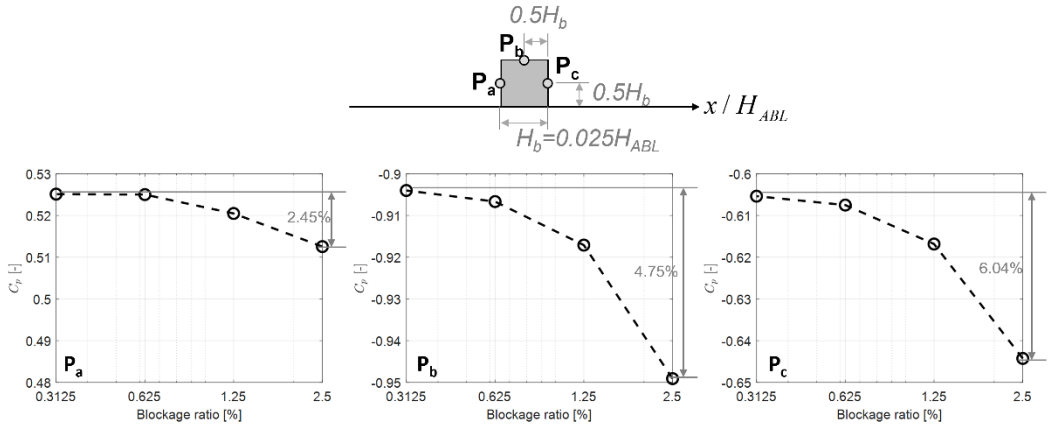

Fig. 20. Change in nondimensional pressure at three points on building facades with respect to blockage ratio.

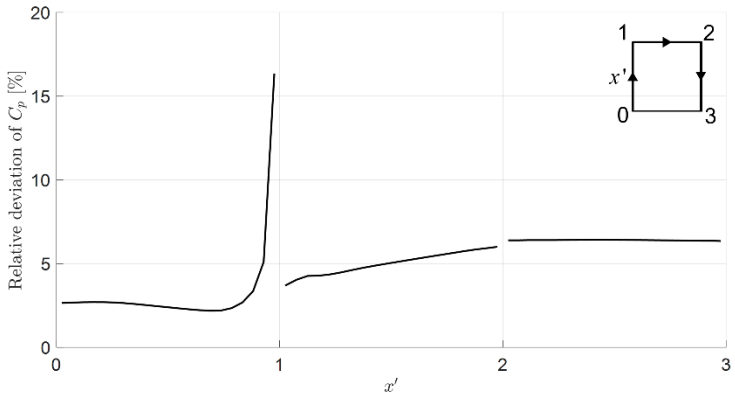

Fig. 21. Relative deviation of pressure coefficient on building façade between two simulations with blockage ratio of 2.5 % and 0.3125 %, i.e., $(C_{p,2.5\%} - C_{p,0.3125\%})/C_{p,0.3125\%}$ x 100%

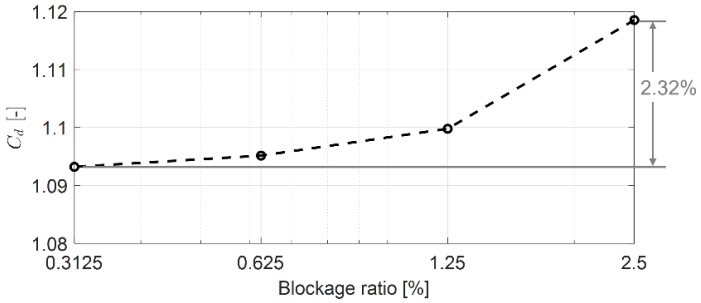

Fig. 22. Change in drag coefficient C_d with respect to blockage ratio.

4.4. Test case 4: topographic flow

This section circles back to the original question of this research, i.e., how can we simulate topography at large scale without having significant blockage effects and generate approach flow for such simulations. The approach flow conditions developed in Section 4.1 are applied to a simulation with generic topographic features. The first subsection describes the topographic model considered in the current section as well as simulation setups. The following subsection presents the simulation results and analyses.

4.4.1. Topographic model and CFD simulation setup

The current section simulates two distinct topographic features: a ridge and a plateau. They are mathematically expressed with the following equations:

Ridge:
$$z(x) = H_t \cos^2\left(\frac{\pi}{2H_t}x\right) \quad \text{for } -H_t \le x \le H_t \tag{17}$$

and

Plateau:
$$z(x) = \begin{cases} H_t \cos^2\left(\dfrac{\pi}{4H_t}x\right) & \text{for } -2H_t \le x \le 0 \\ H_t & \text{for } 0 \le x \le 4H_t \\ H_t \cos^2\left(\dfrac{\pi}{H_t}(x-4H_t)\right) & \text{for } 4H_t \le x \le 4.5H_t \end{cases}, \tag{18}$$

where H_t is the height of both the ridge and the plateau models. The ridge is symmetric with respect to the x-axis, while the plateau has a shallow slope, a flat top and a steep slope as shown in Fig. 23. Along the x axis, half of the ridge's length is H_t, and the lengths of the shallow slope, the flat top, and the steep slope of the plateau are $2H_t$, $4H_t$ and $0.5H_t$, respectively. We modeled the height of both topographic features with $H_t = 0.05H_{ABL}$ in the computational domain of H_{ABL}, $2H_{ABL}$, $4H_{ABL}$ and $8H_{ABL}$, which result in blockage ratios of 5 %, 2.5 %, 1.25 % and 0.625 %, respectively.

The setup of simulations in this section is similar to that of the isolated building simulation in Section 4.3. The primary difference is the replacement of the geometry of the building with the generic topography and the modification of the computational grid around the model. Figure 24 depicts the schematics of the simulation domain with the mesh near the geometry of interest. As the geometry becomes more complex than a square-shaped building in the previous section, the grids are finer in the vicinity of the topography such that the important flow features in the region can be correctly captured. Note that the boundary conditions for the bottom wall are consistent for both the flat ground and the surface of the topographic models as this study aims to investigate the impact of large-scale topography. The rest of boundary conditions are summarized in Table 4. The reference pressure is set to 0 at $H = H_{ABL}$ on the inlet boundary regardless of the domain height. Based on the observation in Sections 4.2.2 and 4.3.2, all simulations in this section were conducted by specifying the body force within the ABL height.

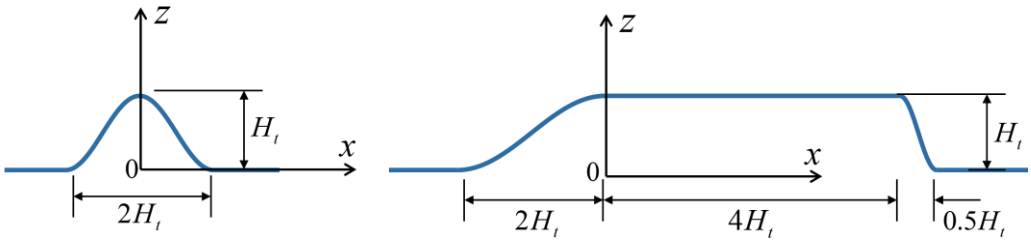

(a) 2D ridge (b) 2D plateau

Fig. 23. Representation of topographic features for the generic model; (a) ridge and (b) plateau

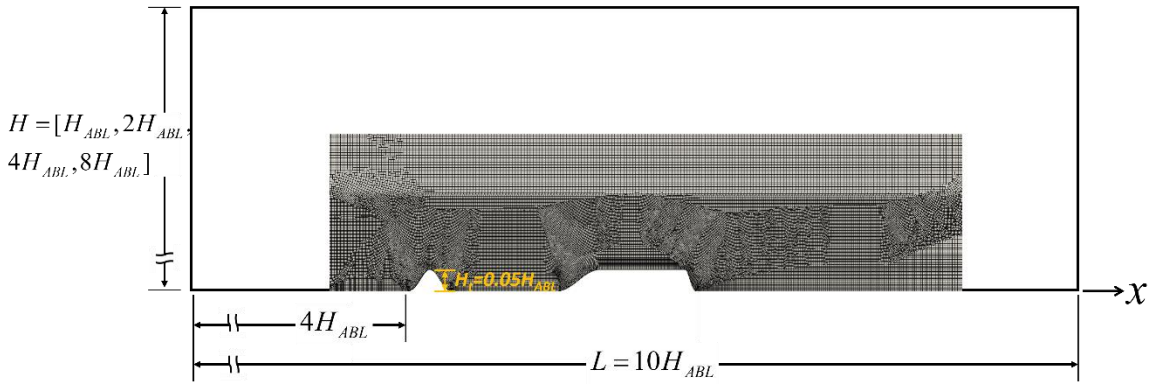

Fig. 24. Mesh view of generic model

Table 4. Boundary conditions of the simulation with generic model

	Inlet	Outlet	Top	Bottom
$\boldsymbol{U}$	fixedValue (from precursor)	zeroGradient	slip	$\|\boldsymbol{U}\|=0$
p	zeroGradient	zeroGradient	slip	zeroGradient
k	fixedValue (from precursor)	zeroGradient	slip	kqRWallFunction
ε	zeroGradient	zeroGradient	slip	epsilonWallFunction
ν_t	zeroGradient	zeroGradient	slip	nutkAtmRoughWallFunction, z_0 = 0.03 m in FS

4.4.2. Results

Figure 25 presents the nondimensional velocity and TKE in the vertical plane from the simulation with $H = H_{ABL}$. The approach flow separates at the top of the ridge, causing the leeward side of the ridge to be covered by its wake. The separated flow extends to the plateau downstream, resulting in a significantly reduced wind speed between the ridge and the plateau compared to the other locations. The wake that forms behind the plateau is not as strong as the one that forms behind the ridge. The U, k, and ε fields show negligible differences within the ABL height in the simulations with different domain heights of H_{ABL}, $2H_{ABL}$, $4H_{ABL}$ and $8H_{ABL}$. As observed in the simulations with the empty domain and with an isolated building in the previous sections, the predictions of U and k fields by the other simulations with different domain heights compare well to the showcased results in the figure unlike the pressure field. The blockage effect was quantitatively investigated by comparing the field quantities from the simulations with different blockage ratio of 0.3125 %, 0.625 %, 1.25 % and 2.5 %. Figure 26 first presents the distribution of relative deviation in velocity magnitude and TKE, and simple deviation of pressure coefficient between the two cases with the maximum and minimum blockage ratio, like Fig. 21 in the previous section. Again, the lowest blockage simulation is used as a reference for the calculation of the relative deviation, given that the case would produce the solution the least affected by the domain size. Similar to the comparison for an isolated building case, the blockage effect on velocity and TKE fields are not significant, and the maximum relative deviation of both quantities fall below 5 %. Because the height of the generic topography is two times greater than that of the single building tested previously, the blockage effect is more pronounced and the relative deviation is also higher than the case with a smaller structure. Figure 27 shows the change of nondimensional velocity, TKE and pressure at four locations P_1 through P_4 that are horizontally distanced by $0.2H_{ABL}$ to their adjacent points and vertically spaced by H_t from the four points of interest on the ground. The projection of points P_1 through P_4 onto the ground corresponds to the apex of the ridge, in the middle of the wake region behind the ridge, the top of the nose of the plateau, and the trailing edge of the plateau, respectively. The amount of change of field quantities varies by the location of the sampling point and the field variable itself. The comparison of the nondimensional pressure to the velocity and TKE confirms that the pressure field is more sensitive to the blockage effect than the two other fields: the mean percent deviation of p is 19.62 % by the change of blockage ratio from 5 % to 0.625 % while that of U and k are only 3.10 % and 1.88 %, respectively. Next, the changes of pressure sampled at the four points P_a through P_d on the topography are presented in Fig. 28. The average change of pressure at the four points is 13.73 % and this number is smaller than the variation of pressure sampled at the points H_t above the ground, i.e., P_1 to P_4. Those results are consistent with the conclusion made with the simulations of an isolated building in the previous section and confirm that the blockage ratio should be reduced to avoid the unintended blockage effect particularly when the pressure on a structure or over topography is of primary interest. Figure 29 presents the relative deviation in velocity magnitude and TKE along the line constantly distanced by H_t from the topography, as well as the difference in pressure coefficient on the surface of the topography. The results agree well with the observations in other simulation results, showing significant impact of blockage on pressure with minute effects on the velocity and TKE fields. The pressure coefficient varies by at least 0.02 due to the change in domain height with the peak variations of 0.151 at the top of the ridge and -0.099 at the trailing edge of the plateau, respectively. Given that the impact of blockage on U and k is minute, it would be not critical to use a vertically extended computational domain and to pursue low blockage ratio, if only the velocity and TKE

fields are of concern but not the pressure. Note that the simulations in the current study were conducted in 2D settings and that the required blockage ratio that does not produce significant changes in pressure may be different in 3D simulations.

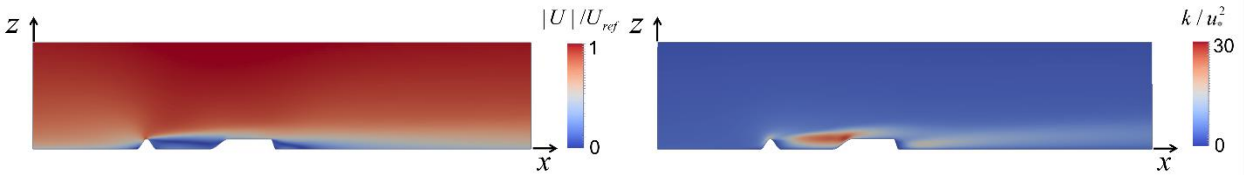

(a) Velocity magnitude (b) Turbulence kinetic energy

Fig. 25. Contour of non-dimensional velocity magnitude and turbulence kinetic energy around the topography of interest.

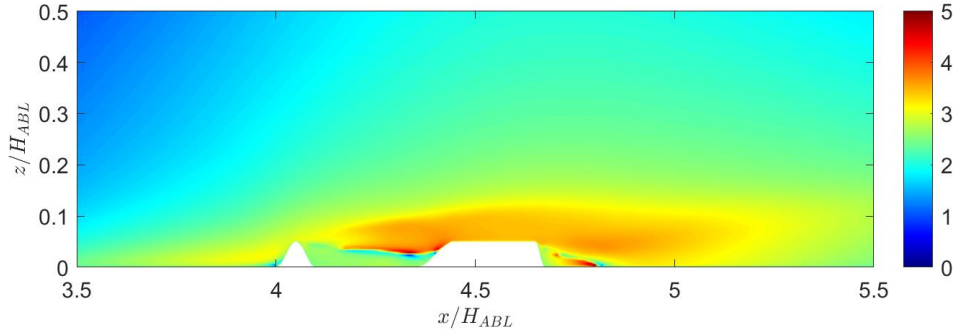

(a) Relative deviation of velocity magnitude [%]

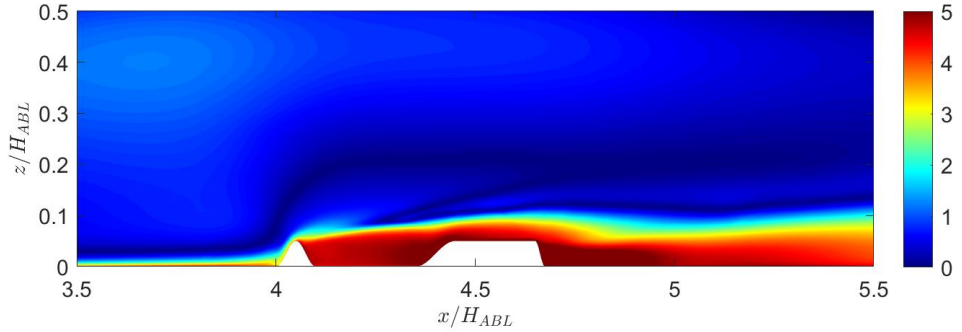

(b) Relative deviation of TKE [%]

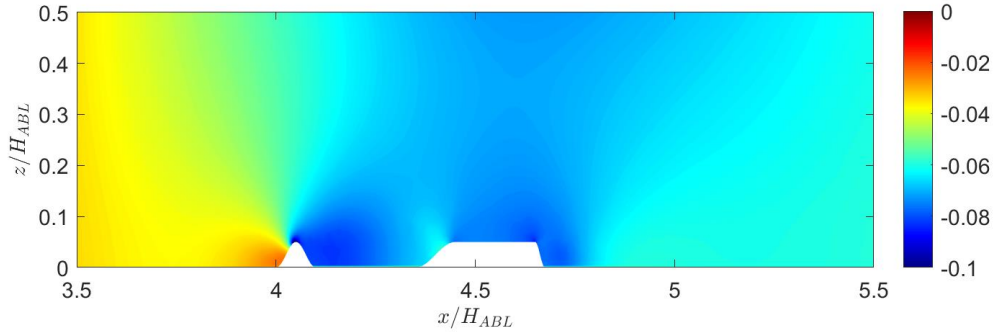

(c) Difference in pressure coefficient [-]

Fig. 26. Distribution of relative deviation in (a) velocity magnitude and (b) TKE; and (c) difference in pressure coefficient; between the two simulations with the blockage ratio of 5 % and 0.625 % with using the lowest blockage case as reference for the relative deviation

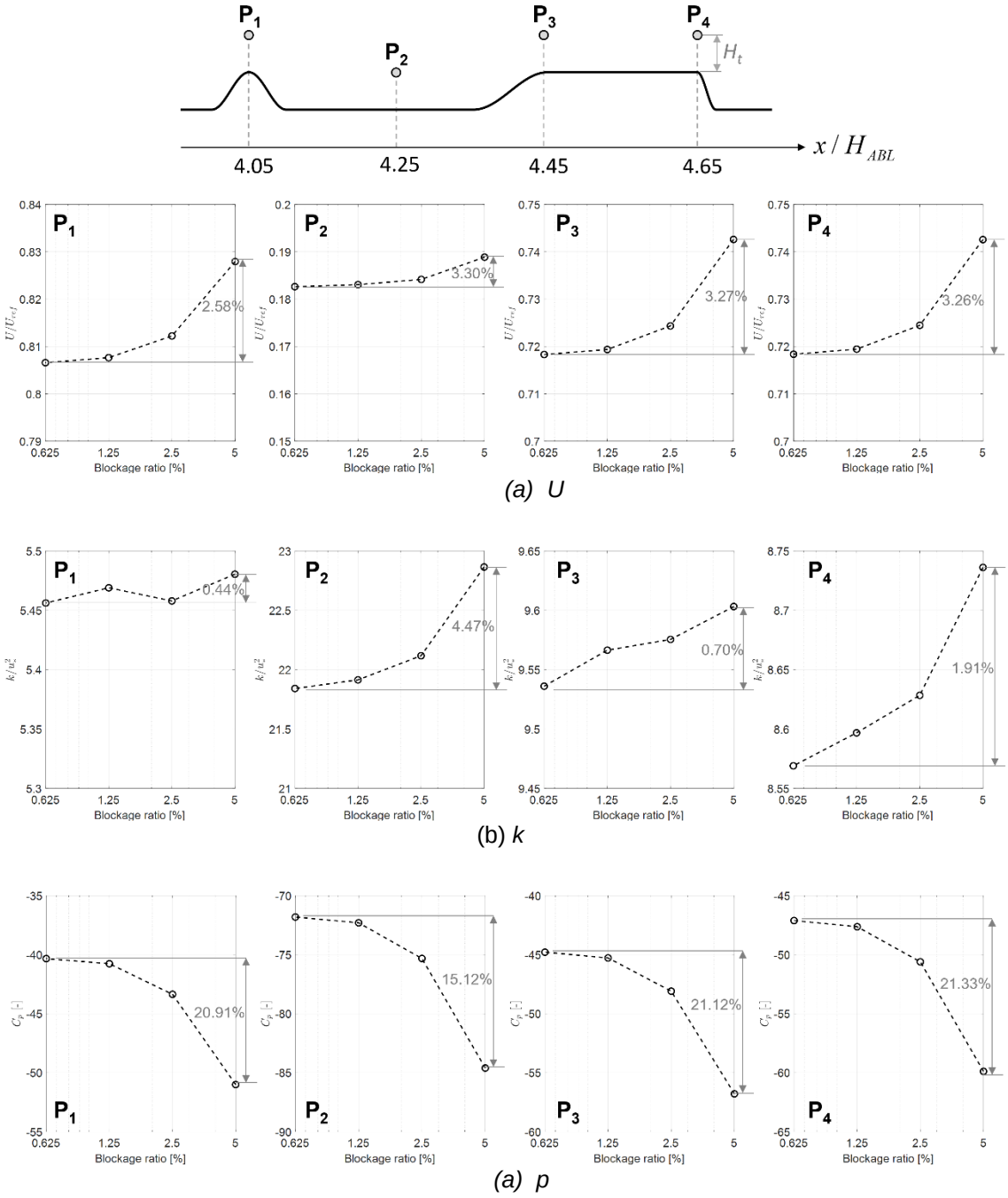

Fig. 27. Effects of blockage ratio on flow field above topography.

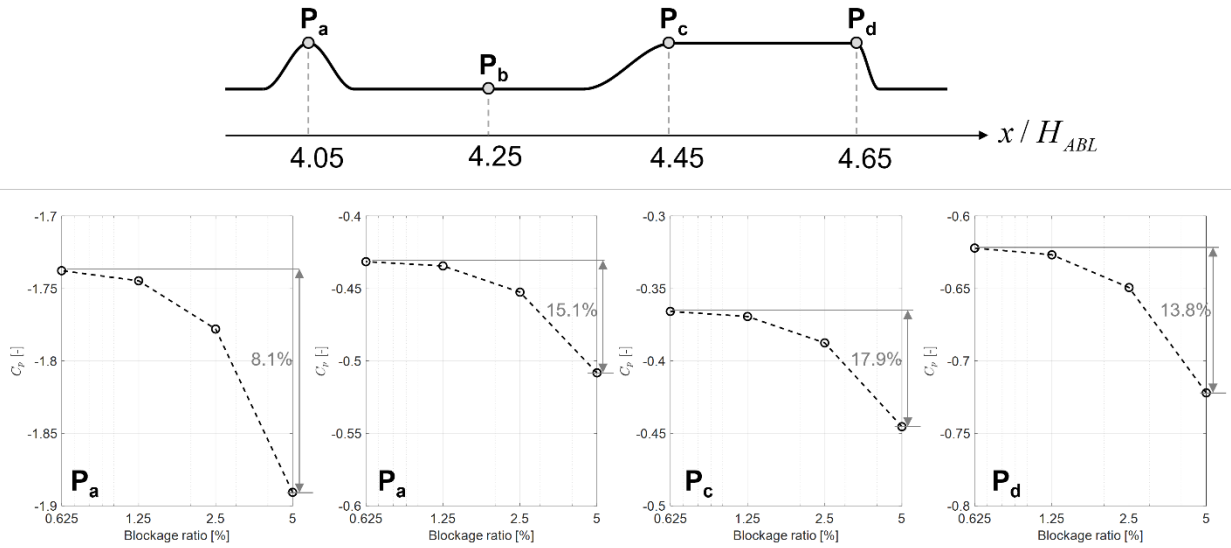

Fig. 28. Change of nondimensional pressure at four locations on the ground surface with respect to the blockage ratio.

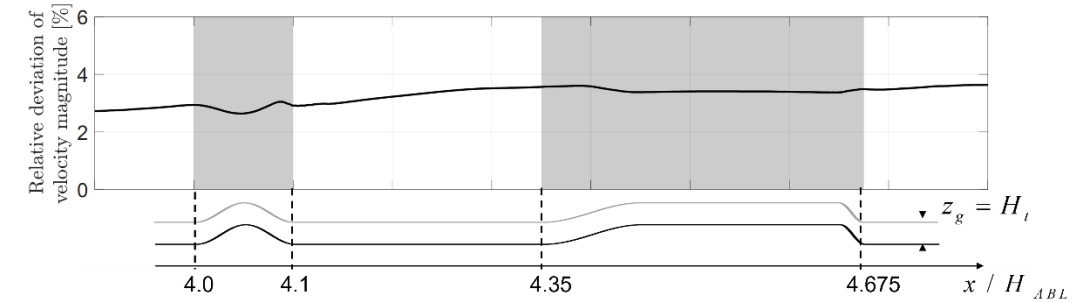

(a) Relative deviation of velocity magnitude [%]

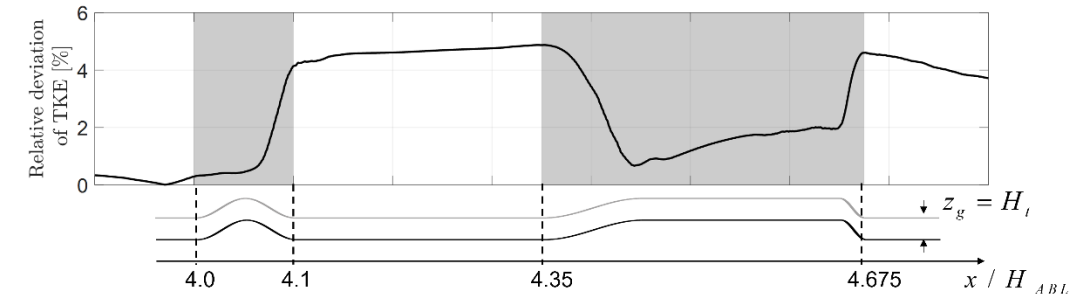

(b) Relative deviation of TKE [%]

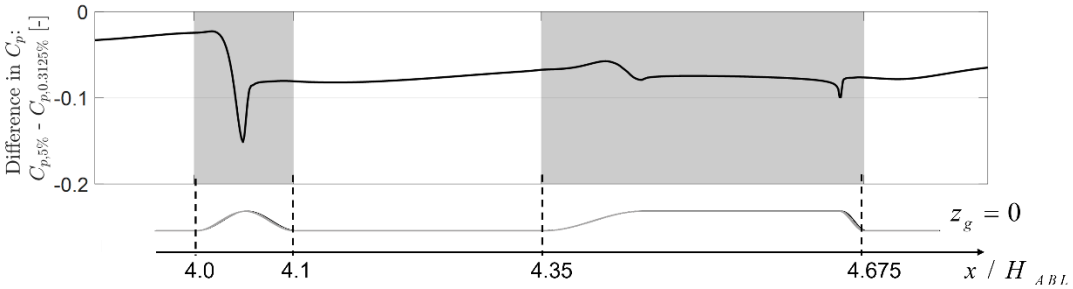

(c) Difference in pressure coefficient [-]

Fig. 29. Relative deviation in (a) velocity magnitude and (b) TKE along the line distanced from the terrain by z_g=H_t, and in (c) pressure on the topography.

5. Proposed CFD procedure for ABL approach flow in wind engineering applications

This section summarizes the CFD procedure proposed in this study for the generation of an ideal approach flow in structural wind engineering applications, based on the findings from the test case simulations in the previous sections. For accurate estimation of flow fields around and associated wind loads on a structure, it is imperative to generate an ideal approach flow that satisfies the following characteristics: a fully developed flow featuring horizontal homogeneity, zero streamwise pressure gradient, and a realistic shear stress profile within the ABL height. Also, for structural engineering application purposes, adaptability to extend the domain vertically beyond the ABL height is required to have an acceptably low blockage effect in large-scale simulations (e.g., with buildings in urban and/or topographic environments). To develop approach flow that satisfies these requirements, we theoretically explained our method in Sec. 3 and confirmed with the test-case simulations in Sec. 4 that a body force, derived from a target shear stress profile, needs to be incorporated within the ABL height in a domain to drive the ABL flow.

The proposed procedure necessitates a precursor simulation with a body force to obtain the ABL flow with the desired flow characteristics in terms of its aerodynamic roughness length, friction velocity, and the streamwise wind speed at a reference height. The target shape of the shear stress profile for the ABL determines the body force profile, and ultimately, the ABL flow profiles. These achieved profiles from the precursor are applied to a main simulation where a model of interest (e.g., such as a building and topographic surroundings) is located in the domain for structural engineering applications. In the main simulation, the body force used in the precursor simulation should also be employed. Otherwise, a horizontal pressure gradient, equivalent to the missing body force, automatically builds up throughout the domain. Since this undesired gradient is embedded in the pressure field in the domain, its influence on the pressure field should be eliminated for accurate estimation of pressure (e.g., on a building of interest). Note that the flow velocity and TKE fields, commonly of main interest in environmental wind engineering applications, are identical in the main simulations with and without the body force.

For simulations whose domain height is higher than the ABL height, the role of the body force is particularly important. Without the body force, the horizontal homogeneity of profiles significantly deteriorates along the streamwise direction because the automatically generated pressure gradient cannot perfectly replace the role of the body force within the ABL height as a driving force.

The proposed approach enables lowering of the blockage ratio in a main simulation by vertically extending the domain size beyond the ABL height while maintaining all flow characteristics unchanged within the ABL. This feature is needed to avoid any disturbance of flow and aerodynamic characteristics of interest, particularly for large-scale simulations including buildings in urban environment and/or over topographic surroundings (e.g., ridges and mountains). Otherwise, corrections are required.

6. Conclusion

Previous studies using computational fluid dynamics (CFD) in structural wind engineering have made efforts on developing an ideal approach flow (i.e., a fully developed flow characterized by horizontal homogeneity, zero streamwise pressure gradient and a realistic shear stress profile) for the accurate estimation of wind loads on a structure. However, those studies have focused on a computational domain whose height is equal to or less than the ABL height, in spite of the necessity for the approach flow in computational domains taller than the atmospheric boundary layer (ABL) height.

In this study, we proposed a practical method for generating the ideal approach flow in the computational domain that encompasses the free atmosphere beyond the ABL height to ensure an acceptably low blockage effect on flow quantities. The ideal approach flow profiles were successfully generated in a precursor simulation with vertically extended domain beyond the ABL height by using the body-force-driven approach, then the profiles were applied to main simulations of a horizontally elongated empty domain, and with an isolated building and topographic models. We identified that the body force should be incorporated in the main simulations to satisfy all the requirements, otherwise an undesired pressure field automatically builds up throughout the domain to replace the missing body force that originally generated the profiles, and would result in inaccurate pressure distribution on a model's surfaces. The investigation of velocity (U), turbulence kinetic energy (k) and pressure fields with respect to blockage ratio indicated that the pressure is more vulnerable to the blockage effect than the other two: the average percent change of the pressure at specific locations of interest were approximately order of magnitude higher than that of U and k. One crucial advantage of the proposed method is that the blockage ratio can be substantially reduced by increasing the height of computational domain to avoid unintended blockage effects on the pressure fields on a structure. The proposed approach would be an optimal method for simulations where the blockage ratio cannot be reduced by laterally extending the computational domain. Although the current study employed the Reynolds-Averaged Navier-Stokes (RANS) approach in a 2-D setting to demonstrate the procedure development, the approach is not limited only to RANS modeling but is applicable to 3-D simulations with higher fidelity technique like large-eddy simulations (LES). Therefore, future work will include application of the proposed approach to 3D simulations with complex topography for validation of the procedure.

7. References

Anderson, W. & Meneveau, C., 2011. Dynamic roughness model for large-eddy simulation of turbulent flow over multiscale, fractal-like rough surfaces. *Journal of Fluid Mechanics,* Volume 679, pp. 288-314.

ASCE, 2017. *ASCE/SEI 7-16, Minimum Design Loads and Associated Criteria for Buildings and Other Structures.* Reston, VA: ASCE.

ASCE, 2021. *ASCE/SEI 49-21, Wind tunnel testing for buildings and other structures.* Reston, VA: ASCE.

Cai, X., Huo, Q., Kang, L. & Song, Y., 2014. Equilibrium atmospheric boundary-layer flow: computational fluid dynamics simulation with balanced forces. *Boundary-layer meteorology,* 152(3), pp. 349-366.

Cindori, M., Džijan, I., Juretić, F. & Kozmar, H., 2020. The atmospheric boundary layer above generic hills: computational model of a unidirectional body force-driven flow. *Boundary-Layer Meteorology,* 176(2), pp. 159-196.

Cindori, M., Juretić, F., Kozmar, H. & Džijan, I., 2018. Steady RANS model of the homogeneous atmospheric boundary layer. *Journal of Wind Engineering and Industrial Aerodynamics,* Volume 173, pp. 289-301.

Deaves, D. & Harris, R., 1978. *A mathematical model of the structure of strong winds,* London: CIRIA Report 76, Construction Industry Research and Information Association.

Franke, J., Hellsten, A., Schlünzen, K. H. & Carissimo, B., 2007. *Best Practice Guideline for the CFD Simulation of Flows in the Urban Environment: COST Action 732 Quality Assurance and Improvement of Microscale Meteorological Models.* Brussels, Belgium: COST Office.

Hargreaves, D. M. & Wright, N. G., 2007. On the use of the k–ε model in commercial CFD software to model the neutral atmospheric boundary layer. *Journal of wind engineering and industrial aerodynamics,* 95(5), pp. 355-369.

IHS ESDU, 2001. *Characteristics of Atmospheric Turbulence Near the Ground—Part II: Single Point Data for Strong Winds (Neutral Atmosphere),* London, UK: Engineering Sciences Data Unit, IHS Inc.,.

Kozmar, H., 2011. Wind-tunnel simulations of the suburban ABL and comparison with international standards. *Wind and Structures, An International Journal,* 14(1), pp. 15-34.

Melbourne, W., 1982. *Wind tunnel blockage effects and correlations.* Cambridge, UK, Cambridge University Press, p. 197–216.

Nandi, T. N. & Yeo, D., 2021. Estimation of integral length scales across the neutral atmospheric boundary layer depth: A Large Eddy Simulation study. *Journal of Wind Engineering and Industrial Aerodynamics,* Volume 218, p. 104715.

OpenFOAM, 2019. *The open source CFD toolbox: User guide (version 7),* s.l.: OpenFOAM Foundation.

Parente, A., Gorlé, C., van Beeck, J. & Benocci, C., 2011a. A comprehensive modelling approach for the neutral atmospheric boundary layer: consistent inflow conditions, wall function and turbulence model. *Boundary-layer meteorology,* 140(3), pp. 411-428.

Parente, A., Gorlé, C., van Beeck, J. & Benocci, C., 2011b. Improved k–ε model and wall function formulation for the RANS simulation of ABL flows. *Journal of wind engineering and industrial aerodynamics,* 99(4), pp. 267-278.

Richards, P. J. & Hoxey, R. P., 1993. Appropriate boundary conditions for computational wind engineering models using the k-ϵ turbulence model. *Journal of wind engineering and industrial aerodynamics,* Volume 46, pp. 145-153.

Richards, P. J. & Norris, S. E., 2011. Appropriate boundary conditions for computational wind engineering models revisited. *Journal of Wind Engineering and Industrial Aerodynamics,* 99(4), pp. 257-266.

Richards, P. J. & Norris, S. E., 2015. Appropriate boundary conditions for a pressure driven boundary layer. *Journal of Wind Engineering and Industrial Aerodynamics,,* Volume 142, pp. 43-52.

Richards, P. J. & Norris, S. E., 2019. Appropriate boundary conditions for computational wind engineering: Still an issue after 25 years. *Journal of Wind Engineering and Industrial Aerodynamics,* Volume 190, pp. 245-255.

Shi, L. & Yeo, D., 2017. Large eddy simulations of model-scale turbulent atmospheric boundary layer flows.. *Journal of Engineering Mechanics,* 143(9), p. 06017011.

Simiu, E. & Yeo, D., 2019. *Wind effects on structures: Modern structural design for wind.* Hoboken, NJ, USA: John Wiley & Sons.

Tominaga, Y. et al., 2008. AIJ guidelines for practical applications of CFD to pedestrian wind environment around buildings. *Journal of wind engineering and industrial aerodynamics,* 96(10-11), pp. 1749-1761.

van der Laan, M., Kelly, M. & Baungaard, M., 2021. A pressure-driven atmospheric boundary layer model satisfying Rossby and Reynolds number similarity. *Wind Energy Science,* 6(3), pp. 777-790.

van der Laan, M., Kelly, M., Floors, R. & Peña, A., 2020. Rossby number similarity of an atmospheric RANS model using limited-length-scale turbulence closures extended to unstable stratification. *Wind Energy Science,* 5(1), pp. 355-374.

Yang, Y., Gu, M., Chen, S. & Jin, X., 2009. New inflow boundary conditions for modelling the neutral equilibrium atmospheric boundary layer in computational wind engineering. *Journal of Wind Engineering and Industrial Aerodynamics,* 97(2), pp. 88-95.

Yeo, D. & Shi, L., 2018. Computational vs. Wind Tunnel Simulation of Atmospheric Boundary Layer Flow for Structural Engineering Applications. In: *Wind Engineering for Natural Hazards: Modeling, Simulation, and Mitigation of Windstrom Impact on Critical Infrastructure.* Reston(VA): ASCE, pp. 169-191.